



AFRL-RQ-WP-TR-2014-0163

LEVERAGING MULTI-FIDELITY MODELS FOR FLEXIBLE WING SYSTEMS

B. Balachandran

University of Maryland, College Park

**MAY 2014
Final Report**

Approved for public release; distribution unlimited

**AIR FORCE RESEARCH LABORATORY
AEROSPACE SYSTEMS DIRECTORATE
WRIGHT-PATTERSON AIR FORCE BASE, OH 45433-7541
AIR FORCE MATERIEL COMMAND
UNITED STATES AIR FORCE**

NOTICE AND SIGNATURE PAGE

Using Government drawings, specifications, or other data included in this document for any purpose other than Government procurement does not in any way obligate the U.S. Government. The fact that the Government formulated or supplied the drawings, specifications, or other data does not license the holder or any other person or corporation; or convey any rights or permission to manufacture, use, or sell any patented invention that may relate to them.

This report was cleared for public release by the USAF 88th Air Base Wing (88 ABW) Public Affairs Office (PAO) and is available to the general public, including foreign nationals.

Copies may be obtained from the Defense Technical Information Center (DTIC)
(<http://www.dtic.mil>).

AFRL-RQ-WP-TR-2014-0163 HAS BEEN REVIEWED AND IS APPROVED FOR
PUBLICATION IN ACCORDANCE WITH ASSIGNED DISTRIBUTION STATEMENT.

*//Signature//

PHILIP S. BERAN
Program Manager
Design and Analysis Branch
Aerospace Vehicles Division

//Signature//

THOMAS C. CO, Chief
Design and Analysis Branch
Aerospace Vehicles Division

*//Signature//

FRANK WITZEMAN, Chief
Aerospace Vehicles Division
Aerospace Systems Directorate

This report is published in the interest of scientific and technical information exchange, and its publication does not constitute the Government's approval or disapproval of its ideas or findings.

*Disseminated copies will show “//Signature//” stamped or typed above the signature blocks.

REPORT DOCUMENTATION PAGE					Form Approved OMB No. 0704-0188	
<p>The public reporting burden for this collection of information is estimated to average 1 hour per response, including the time for reviewing instructions, searching existing data sources, gathering and maintaining the data needed, and completing and reviewing the collection of information. Send comments regarding this burden estimate or any other aspect of this collection of information, including suggestions for reducing this burden, to Department of Defense, Washington Headquarters Services, Directorate for Information Operations and Reports (0704-0188), 1215 Jefferson Davis Highway, Suite 1204, Arlington, VA 22202-4302. Respondents should be aware that notwithstanding any other provision of law, no person shall be subject to any penalty for failing to comply with a collection of information if it does not display a currently valid OMB control number. PLEASE DO NOT RETURN YOUR FORM TO THE ABOVE ADDRESS.</p>						
1. REPORT DATE (DD-MM-YY) May 2014		2. REPORT TYPE Final		3. DATES COVERED (From - To) 28 October 2009 – 27 May 2014		
4. TITLE AND SUBTITLE LEVERAGING MULTI-FIDELITY MODELS FOR FLEXIBLE WING SYSTEMS					5a. CONTRACT NUMBER FA8650-10-2-3012	
					5b. GRANT NUMBER	
					5c. PROGRAM ELEMENT NUMBER 62201F	
6. AUTHOR(S) B. Balachandran					5d. PROJECT NUMBER 2401	
					5e. TASK NUMBER	
					5f. WORK UNIT NUMBER Q1AT	
7. PERFORMING ORGANIZATION NAME(S) AND ADDRESS(ES) University of Maryland, College Park 2181 Glenn L Martin Hall College Park, MD 20742					8. PERFORMING ORGANIZATION REPORT NUMBER	
9. SPONSORING/MONITORING AGENCY NAME(S) AND ADDRESS(ES) Air Force Research Laboratory Aerospace Systems Directorate Wright-Patterson Air Force Base, OH 45433-7541 Air Force Materiel Command United States Air Force					10. SPONSORING/MONITORING AGENCY ACRONYM(S) AFRL/RQVC	
					11. SPONSORING/MONITORING AGENCY REPORT NUMBER(S) AFRL-RQ-WP-TR-2014-0163	
12. DISTRIBUTION/AVAILABILITY STATEMENT Approved for public release; distribution unlimited.						
13. SUPPLEMENTARY NOTES PA Case Number: 88ABW-2014-4167; Clearance Date: 02 Sep 2014.						
14. ABSTRACT <p>This is the final report for the activities conducted at the University of Maryland during participation in the Collaborative Center in Multidisciplinary Sciences (CCMS) project. In this work, the investigators have primarily explored the suitability of computational tools to predict desirable micro-air-vehicle (MAV) designs. The use of computationally expensive high-fidelity tools such as direct numerical simulation is compared to that of moderate fidelity tools, such as the inexpensive unsteady vortex lattice method. An achievement of the project was the implementation of a high-fidelity fluid-structure interaction simulation code inside the FLASH framework. This tool permits the study of flapping wing systems with high fidelity in three dimensions.</p>						
15. SUBJECT TERMS MAV modeling, flapping systems, fluid-structure interactions						
16. SECURITY CLASSIFICATION OF:			17. LIMITATION OF ABSTRACT: SAR	18. NUMBER OF PAGES 60	19a. NAME OF RESPONSIBLE PERSON (Monitor) Philip S. Beran 19b. TELEPHONE NUMBER (Include Area Code) (937) 713-7217	
a. REPORT Unclassified	b. ABSTRACT Unclassified	c. THIS PAGE Unclassified				

TABLE OF CONTENTS

<u>Content</u>	<u>Page</u>
LIST OF FIGURES	1
LIST OF TABLES	1
1 SUMMARY	2
2 ACADEMIC ACTIVITIES	3
2.1 Supported Personnel.....	3
2.1.1 Faculty.....	3
2.1.2 Graduate Students	3
2.2 Publications	3
2.2.1 Journal Articles	3
2.2.2 Conference papers.....	3
3 Two-Dimensional Modeling.....	4
3.1 Initial study on flexibility	4
3.2 Fluid-structure interactions	6
3.3 Parameterization.....	7
3.4 Direct numerical simulations in two dimensions	9
3.5 Unsteady vortex lattice method in two dimensions	11
3.6 POD analysis of the flow fields.....	12
3.6.1 Formulation.....	12
3.6.2 Results.....	14
3.7 Comparing the results from DNS and UVLM studies	17
3.7.1 Flow fields	17
3.7.2 Aerodynamic loads	20
4 Three-Dimensional Modeling.....	25
4.1 Introduction	25
4.2 Experiments.....	25
4.3 Implementation using geometrically exact finite elements.....	29
4.3.1 Equations of motion.....	30

4.3.2	Application of essential boundary conditions	31
4.4	Fluid-structure interactions	32
4.4.1	Overview	32
4.4.2	Imposition of boundary conditions	33
4.4.3	The Generalized- α method.....	36
5	Moving plate example.....	38
5.1	Formulation	38
5.2	Results	39
6	Concluding Remarks.....	43
6.1	Future work	43
6.2	Outcomes.....	45
7	References	46

LIST OF FIGURES

Figure	Page
Figure 1: Schematic illustration of a two-dimensional wing profile as a representative cross-section of an insect wing.....	4
Figure 2: Schematic of two-dimensional profile with discrete flexibility. (A) Details of the profile's description and coordinates on the 10% thickness case. (B) Example of the 3% thickness case.....	5
Figure 3: Process flow diagram of the fluid-structure coupling scheme.	7
Figure 4: Schematic of the profile inside the DNS grid showing the overall size of the domain. The detailed view shows a close up near the leading edge of a 10% thick body, where the red lines are grid lines, the black points are control points representing the body, and the flow field is the magnitude of velocity for $Re = 250$, $\omega_f / \omega_n = 1/2$, at time $t/T = 9.75$	9
Figure 5: Vorticity contours from DNS at $Re = 75$. Contours range from -10 to 10 with 80 intervals. Columns A-C are flexible profiles with $\omega_f / \omega_n \in \{1/2, 1/3, 1/4\}$, respectively; Column D is the rigid profile. Adapted from Vanella <i>et al.</i> (2009).	10
Figure 6: Averaged lift to drag ratio from the two-dimensional DNS calculations for various frequency ratios. Profile thickness is $l/10$	11
Figure 7: Schematic for the discretization of the Unsteady Vortex Lattice Method.	12
Figure 8: Vorticity contours determined by POD from DNS at $Re = 75$, 10% thickness, and harmonic kinematics. Normalization is $\max_{\mathbf{x}} \nabla \times \phi_i(\mathbf{x}) = 1$. Horizontal scale is x/l , vertical scale is y/l	15
Figure 9: Vorticity contours determined by POD from DNS at $Re = 250$, 10% thickness, and harmonic kinematics. Normalization is $\max_{\mathbf{x}} \nabla \times \phi_i(\mathbf{x}) = 1$. Horizontal scale is x/l , vertical scale is y/l	16
Figure 10: Magnitude of the velocity fields from periods 6--7 for $\omega_f / \omega_n = 1/2$, DNS at $Re \in \{75, 250, 1000\}$, and UVLM. The velocity field is normalized as $ \mathbf{u} _2 / u_{\text{ref}}$	18
Figure 11: Comparisons of Mode 1 of POD velocity contours from DNS and UVLM data for $\omega_f / \omega_n = 1/3$ with harmonic kinematics. The fields are normalized by $\max_{\mathbf{x}} \phi_i(\mathbf{x}) _2 / u_{\text{ref}} = 1$. Horizontal scale is x/l , vertical scale is y/l	19
Figure 12: Time series of the dimensionless loads of the hovering profile from DNS at $Re = 1000$ in red and UVLM in blue for the frequency ratio $\omega_f / \omega_n = 1/3$	21
Figure 13: Phase averaged forces of the hovering profile from DNS at $Re = 1000$ in red and UVLM in blue for various frequency ratios. (a) Lift coefficient and (b) drag coefficient. Adapted from Fitzgerald <i>et al.</i> (2011).	22

Figure 14: Comparisons of time averaged dimensionless lift and drag coefficients from the UVLM and DNS at various Re . (a) Mean lift and drag coefficients, (b) the ratio of mean lift to mean drag. Adapted from Fitzgerald <i>et al.</i> (2011).....	23
Figure 15: Schematic depicting the use of a scanning laser vibrometer to characterize the spectral response of a living insect wing using non-contact excitation.	27
Figure 16: Mesh of the scanning laser vibrometer on a living <i>Manduca sexta</i> forewing. The color markers indicate locations of signal points in Figure 17. Note that $+x$ is in the vertical direction.	27
Figure 17: Normalized magnitude of the FFT of the velocity data determined from the laser vibrometer at various points on the forewing of a <i>Manduca sexta</i> . The color points are indicated on Figure 16.	28
Figure 18: Experimentally determined modes of a living <i>Manduca sexta</i> forewing. The x and y coordinates are scaled by the wing span, z is scaled such that the $\max z/l = 1/8$ for visualization. (A) Mode 1 at 77.5 Hz. (B) Mode 2 at 133.75 Hz.	29
Figure 19: Procedure diagram for the partitioned FSI algorithm.	32
Figure 20: A representative region of fluid particles in the fluid domain, and these same particles in the structural domain. (a) The fluid domain particles are used to represent the kinematics of the body's surface. (b) Likewise, the particles are interpreted by the body as patches of constant applied traction.....	34
Figure 21: Discrete surface element of the body. The triad $\{\hat{\mathbf{n}}, \hat{\mathbf{t}}_1, \hat{\mathbf{t}}_2\}$ is a local set of unit vectors on the patch p , with differential area dA and surface traction \mathbf{f}_f	35
Figure 22: Natural domain of the surface element, showing a single particle patch.	35
Figure 23: Example of the surface stresses acting on the body. These are the instantaneous values at $t/T_f = 2.05$, for $Re = 200$, $\rho/\rho_{\text{fluid}} = 1$. (A) Pressure on the body, with colors corresponding to $C_p/2$. (B) Magnitude of the viscous stress, with colors corresponding to $C_f/2$	39
Figure 24: Position of the center of mass in the deformable plate for $Re = 200$	40
Figure 25: Fluid forces computed at the centroid of the deformable plate for $Re = 200$	41
Figure 26: Demonstration of FSI for a flexible plate with $\rho/\rho_{\text{fluid}} = 1$, and $\omega_f/\omega_l = 1/3$. The time has been nondimensionalized with T_f . Shown are isosurfaces of the Q-criterion and a slice of the z velocity in the $y-z$ plane.	42
Figure 27: Mesh of a <i>Manduca sexta</i> inspired wing. The planform is based on the results of O'Hara and Palazotto (2012). The restrained nodes are at the root in magenta. The free nodes are shown in blue (only the top surface is shown for clarity).	43
Figure 28: Demonstration of the implemented kinematics employing the hawkmoth parameters from Berman and Wang (2007).	44

LIST OF TABLES

<u>Table</u>	<u>Page</u>
Table 1: Relative error values of the phase-averaged loads between the $Re = 1000$ DNS and UVLM results for a range of stiffnesses.	23

1 SUMMARY

The AFRL-VT-WSU-UMD Collaborative Center in Multidisciplinary Sciences (CCMS) was established after a successful proposal developed jointly by Virginia Tech and Wright State University and another one from the University of Maryland.

These proposals were developed in response to a Broad Agency Announcement (BAA PKV-08-09) with the following stated purpose:

The Multidisciplinary Technology Center (MDTC) of AFRL will set up an ongoing partnership by establishing a Collaborative Center in Multidisciplinary Sciences (CCMS). The best fit will be a research team whose expertise strongly complements the AFRL team, as this collaborative effort will be an extension of AFRL's Multidisciplinary Technology Center. Developing a Collaborative Center is expected to increase the agility and responsiveness of AFRL research efforts.

This report contains work carried out at the University of Maryland, from the end of the Fall 2009 semester. Our focus included the following:

1. Develop tools for the study and design of micro-air-vehicles (MAVs).
2. Analyze the physics observed through experiments to determine beneficial phenomena.
3. Compare the utility of models of varying levels of fidelity to see how they affect the design process.

In Section 2, the academic activities of the students are listed, including a list of publications. The development and analysis of two-dimensional (2D) flapping models are discussed in Section 3. Special attention is given to comparison of results from the DNS and UVLM models. Novel vibration experiments carried out with the wings of living hawkmoths are included in Section 4, along with a formulation of a highly flexible three-dimensional (3D) solid model for use in FSI. This section also contains a discussion of the fluid-structure interaction (FSI) implementation of the FSI algorithm inside high-performance FLASH code. Numerical demonstrations of the effectiveness of the implementation are presented in Section 5. Finally, concluding remarks are collected together in Section 6.

2 ACADEMIC ACTIVITIES

2.1 Supported Personnel

2.1.1 Faculty

- B. Balachandran, Professor, Department of Mechanical Engineering, University of Maryland, College Park, MD
- E. Balaras, Professor, Department of Bioengineering, University of Maryland, College Park, MD – Investigator moved to the Department of Aerospace and Mechanical Engineering, The George Washington University during the course of the project.

2.1.2 Graduate Students

- T. Fitzgerald, PhD, University of Maryland College Park, “Nonlinear fluid-structure interactions in flapping wing systems,” Fall 2013.
- M. Vanella, PhD, University of Maryland College Park, “A fluid-structure interaction strategy with application to low Reynolds number flapping flight,” Spring 2010.

2.1.3 Journal Articles

- Fitzgerald, T., M. Valdez, M. Vanella, E. Balaras, and B. Balachandran. “Flexible Flapping Systems: Computational Investigations into Fluid-Structure Interactions.” *The Aeronautical Journal* Vol. 115, Issue 1172, October 2011.

2.1.4 Conference papers

- Fitzgerald, T., M. Vanella, E. Balaras, and B. Balachandran. “Partitioned Fluid-Structure Interaction Scheme for Bodies with High Flexibility.” In *66th Annual Meeting of the Division of Fluid Dynamics*, Vol. 58. Pittsburgh, Pennsylvania: American Physical Society, 2013.
- Chabalko, C., T. Fitzgerald, and B. Balachandran. “GPGPU Implementation and Benchmarking of the Unsteady Vortex Lattice Method.” In *51th AIAA Aerospace Sciences Meeting*. Grapevine, Texas, 2013.
- Valdez, M., C. Chabalko, T. Fitzgerald, and B. Balachandran. “Flapping Aerodynamics in Ground Effect.” In *50th AIAA Aerospace Sciences Meeting*. Nashville, Tennessee, 2012.
- Fitzgerald, T., M. Valdez, S. Preidikman, and B. Balachandran. “Thin Flapping Wings: Structural Model and Fluid-Structure Interactions.” In *51st AIAA/ASME/ASCE/AHS/ASC Structures, Structural Dynamics, and Materials Conference*. Orlando, Florida, 2010.
- Fitzgerald, T., M. Valdez, and B. Balachandran. “Flexible Hovering Wing Motions: Proper Orthogonal Decomposition Analysis.” In *48th AIAA Aerospace Sciences Meeting*. Orlando, Florida, 2010.

3 Two-Dimensional Modeling

As an initial step towards understanding phenomena associated with flapping wings and tools that can be used to study these systems, two-dimensional (2D) systems are considered. In a 2D setting, the complicated three-dimensional (3D) motions are idealized to motions of a representative cross-section of a wing, as depicted in Figure 1. This simplification greatly reduces the complexity of the physics, the possible parameter space for exploration, and the associated computational costs. By working with 2D models, the investigators gained a basis to understand the types of models, which would need to be constructed for the 3D cases to be studied later.

3.1 Initial study on flexibility

In the first model studied, a single measure for the chord-wise deflection is used. Here, there are two rigid elements connected at point b by a torsion spring, as depicted in Figure 2. This torsion spring is assumed to be linear with respect to the deflection angle α between the two rigid elements. The location of point b is specified by the coordinates (x, y) , and θ is the orientation of link B. The center of mass m_i , $i \in \{A, B\}$, of each link is located a distance η_i from the connection point b. The length of the profile is l .

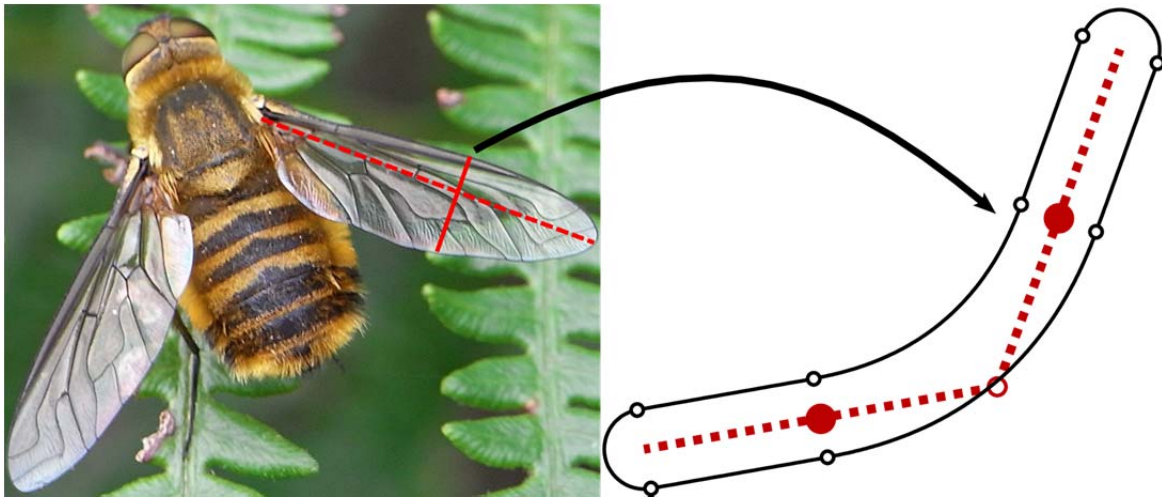


Figure 1: Schematic illustration of a two-dimensional wing profile as a representative cross-section of an insect wing¹.

¹ Photo of female *Villa hottentotta*, used under a Creative Commons Attribution-ShareAlike license, http://commons.wikimedia.org/wiki/File:Villa_hottentotta_female.jpg

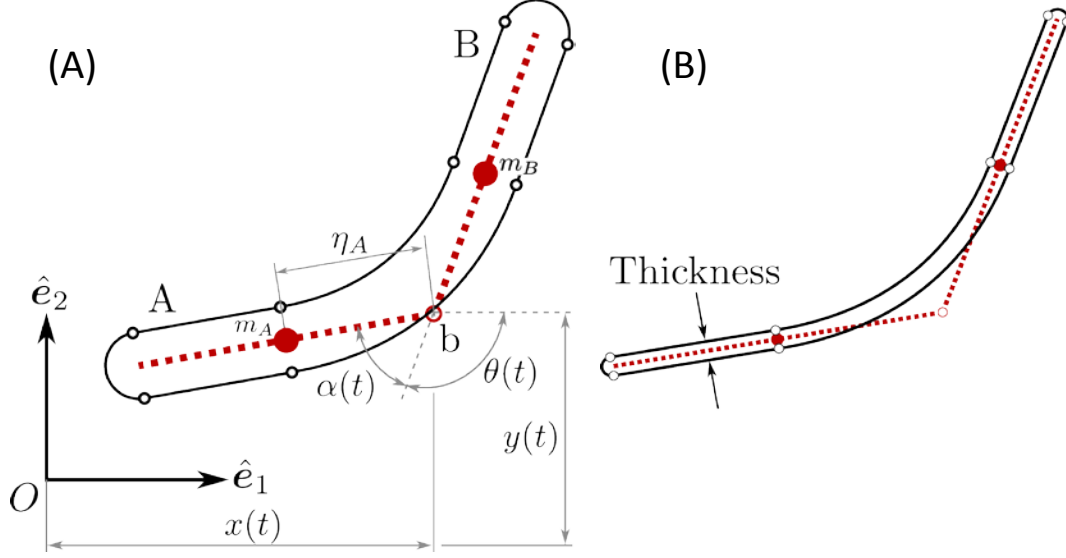


Figure 2: Schematic of two-dimensional profile with discrete flexibility. (A) Details of the profile's description and coordinates on the 10% thickness case. (B) Example of the 3% thickness case.

The equations of motion for this structural model can be arranged as

$$\begin{bmatrix} m_A + m_B & 0 & m_B \eta_B \sin \theta - m_A \eta_A \sin(\alpha + \theta) & -m_A \eta_A \sin(\alpha + \theta) \\ & m_A + m_B & m_B \eta_B \cos \theta - m_A \eta_A \cos(\alpha + \theta) & m_A \eta_A \cos(\alpha + \theta) \\ & & I_A + I_B & I_A \\ \text{symm.} & & & I_A \end{bmatrix} \begin{bmatrix} \ddot{x} \\ \ddot{y} \\ \ddot{\theta} \\ \ddot{\alpha} \end{bmatrix} = \begin{bmatrix} Q_x + g_x \\ Q_y + g_y \\ Q_\theta + g_\theta \\ Q_\alpha + g_\alpha \end{bmatrix} \quad (3.1)$$

where the Q_j , $j \in \{x, y, \theta, \alpha\}$, are the external generalized forces, and g_j are the nonlinear contributions of centrifugal, elastic, and gravity forces. For the case of hovering flight, the motion point b is prescribed. The kinematics of $(x(t), y(t), \theta(t))$ are prescribed functions of time. This reduces the unknowns of (3.1) to a single equation for $\alpha(t)$. This system, which governs the evolution of the deformation of the profile, has the form of a nonlinear oscillator; that is,

$$I_A \ddot{\alpha} + k\alpha = -I_A \ddot{\theta} + m_A \eta_A \ddot{x} \sin(\alpha + \theta) + Q_\alpha. \quad (3.2)$$

This equation does not contain any structural damping since no assumptions have been made about a particular damping model. A consequence of this choice is that this model cannot be excited at (linear) resonance. Combes and Daniel (2003a, 2003b) proposed that certain insects flap their wings near linear resonance, and they applied an arbitrary proportional damping to make a finite element model response match their data. The damping factor used in the work of

Combes and Daniel (2003a) is reported to be 10 times the mass. If that same factor was used to impose linear damping in this model, the system would be overdamped. This level of damping would dominate the response and the interesting interactions with the fluid would be removed. In addition, structural damping data reported in the literature has been limited; there is not yet enough evidence to support a particular material damping model. In the current investigation, the researchers are primarily interested in the elastic response of the flapping system with fully coupled FSI, and significant damping may reduce the influence of aerodynamic forces making the response structurally dominated. Therefore, structural damping is not considered at this stage but is left as possible addition in future work.

3.2 Fluid-structure interactions

The computation of dynamics of the fluid field was carried out by using two models in conjunction with the structural model defined in §3.1. The first one was based on the direct numerical simulation (DNS) of the Navier-Stokes equations for incompressible flows, and the second fluid model used was based on the unsteady vortex lattice method (UVLM).

The coupling scheme is a predictor-corrector method (Preidikman, 1998; Yang *et al.*, 2008), as outlined in Figure 3. Although not monolithic, the main benefit to this strategy is that fluid model and structural model can be modular and replaced as needed. The fluid system is coupled to the structural system by computing the resultant forces from the pressure and vorticity on the surface of the body. This force is then used to integrate a predicted set of structural states. In this predicted configuration, the surface kinematics of the body is fed back as the immersed boundary conditions to the fluid model. This cycle of communication is iterated until the change between sub-steps is below a set tolerance. For all of the models used, only 1 or 2 sub-iterations are found to be needed. This is likely due to the small time steps used to comply with the Courant-Friedrichs-Lewy condition (CFL) number. This approach provides a systematic means to couple the equations of motion in strong form.

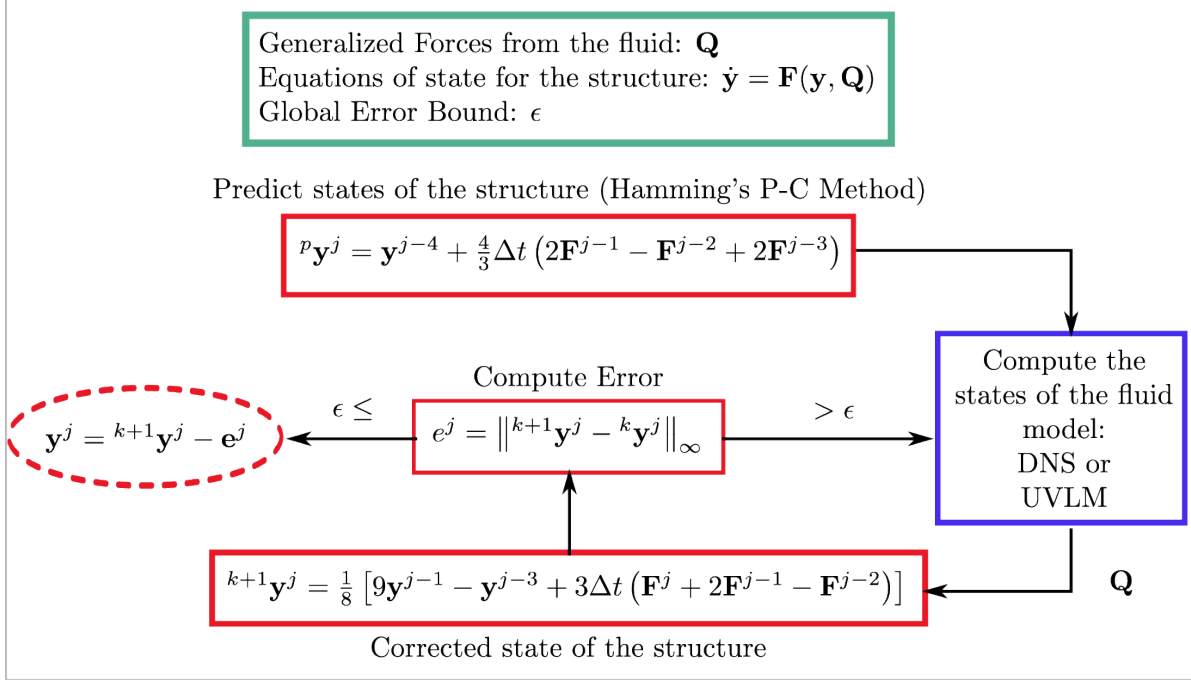


Figure 3: Process flow diagram of the fluid-structure coupling scheme.

3.3 Parameterization

The kinematics used are based on simple harmonic hovering (Wang *et al.*, 2004). These have been adapted to include a non-impulsive start (Vanella *et al.*, 2009).

$$\begin{aligned}
 x(t) &= (1 - e^{-t/\tau}) \frac{A_x}{2} \sin(\omega_f t) \\
 y(t) &= 0 \\
 \theta(t) &= \theta_0 + (1 - e^{-t/\tau}) A_\theta \sin(\omega_f t + \phi) \\
 \tau &= 0.8 \left(\frac{2\pi}{\omega_f} \right)
 \end{aligned} \tag{3.3}$$

Here $(x(t), y(t), \theta(t))$ are the location and orientation of the top segment of the profile shown in Figure 2. The exponential-decay factor is used to prevent the numerical noise from an impulse start. This was found to be beneficial in removing start up noise in the simulations and having the flow fields remain well behaved through the initial transients. The value of τ is chosen so that it takes around 5 periods of hovering to achieve the regular full motion.

The nondimensionalization of the system's parameters reduces the parametric space to 4 key ratios: $(Re, \frac{\rho_{\text{body}}}{\rho_{\text{fluid}}}, \frac{\omega_f}{\omega_n}, \frac{A_x}{l})$. The reference speed of the Reynolds number ($Re = u_{\text{ref}} l / \nu$) is chosen to be the peak translation speed of the forcing

$$\max \dot{x} = \frac{A_x \omega_f}{2}.$$

The reference length is the chord l . The ratio between the stroke length and the chord length is obtained from (Wang *et al.*, 2004) to be $A_x / l = 2.8$. The maximum value for rotation is set to $A_\theta = \pi / 4$, and the profile is assumed to rotate about the vertical position $\theta_0 = -\pi / 2$. For symmetric hover $\phi = 0$, and there is no lead or lag. Fixing $u_{\text{ref}} = 1$, and $l = 1$ provides a period of $T = 2.8\pi$.

The density of the fluid, in the nondimensional DNS code is already 1; so to set the Reynolds number, the kinematic viscosity ν is selected. The parameters of the structure (η_A, m_A, I_A, k) from (3.2) are computed by geometry and choice of $(\frac{\rho_{\text{body}}}{\rho_{\text{fluid}}}, \frac{\omega_f}{\omega_n})$. In Figure 2, each rigid link is taken to be a rectangle with a circular endcap. Due to computational considerations in the fluid solver, a finite thickness profile is needed. The area, location of the centroid η_A , mass m_A , and rotary moment of inertia I_A can be directly computed from geometry once the density ratio is chosen. Finally, the spring constant k is computed from the relation

$$\omega_n^2 = \frac{k}{I_A}.$$

In the next sub-sections, the results obtained through the DNS and UVLM computations are introduced and discussed. For these computations, the ratio $\rho_{\text{body}} / \rho_{\text{fluid}} = 25$ has been chosen to scale the aerodynamic forces to be of the same order as the fluid forces. The fluid-structure interactions are investigated by selecting various spring constants in the model. As discussed above, the difference spring values correspond to different choices of the ratio ω_f / ω_n . In the following results, the values of ω_f / ω_n range from the soft case corresponding to the ratio of 1/2, to the intermediate spring constants of 1/3 and 1/4, and the almost rigid spring case corresponding to $\omega_f / \omega_n = 1/6$.

3.4 Direct numerical simulations in two dimensions

Direct numerical simulation (DNS) represents the highest fidelity computational fluid model in common use. It is constructed by the direct discretization on a staggered grid of the Navier-Stokes equations for incompressible flow. The results, as presented in Vanella *et al.* (2009), are constructed from a second order central difference scheme on a stretched Cartesian mesh. Time marching is performed by using the fractional step method (Kim and Moin, 1985). The body is represented in the fixed grid by using an immersed boundary method (Yang *et al.*, 2008). To enforce the no-slip condition, the predicted velocity field of the fractional step method is forced to match the velocity field along the surface of the body. The flapping profile is placed in the center of a large box so that the boundaries do not interact with the body. The equations are integrated from rest to 15 periods of motion. It takes approximately 1.5 days to compute a single period T of flapping motion on an Intel XEON based computer.

The computational grid was constructed to resolve the boundary layers, and other flow features on the moving profile. A schematic of the domain is shown in Figure 4 with an expanded view near the tip of the body. The center point of the profile is located at the center of a $30l \times 30l$ domain to minimize the effects of the far-field boundary conditions. The center region, where the body passes through, is a uniform grid with cell size $\Delta x = \Delta y = 3.725 \times 10^{-3} l$. This provides approximately 8 or 16 points inside the boundary for the various Reynolds number cases. Outside of this region, the grid is stretched to the boundaries.

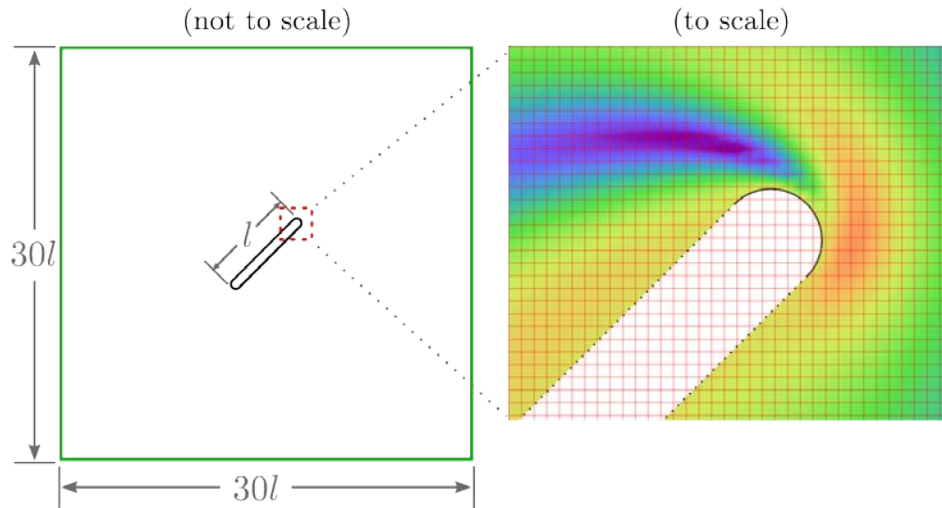


Figure 4: Schematic of the profile inside the DNS grid showing the overall size of the domain. The detailed view shows a close up near the leading edge of a 10% thick body, where the red lines are grid lines, the black points are control points representing the body, and the flow field is the magnitude of velocity for $Re = 250$, $\omega_f / \omega_n = 1/2$, at time $t/T = 9.75$.

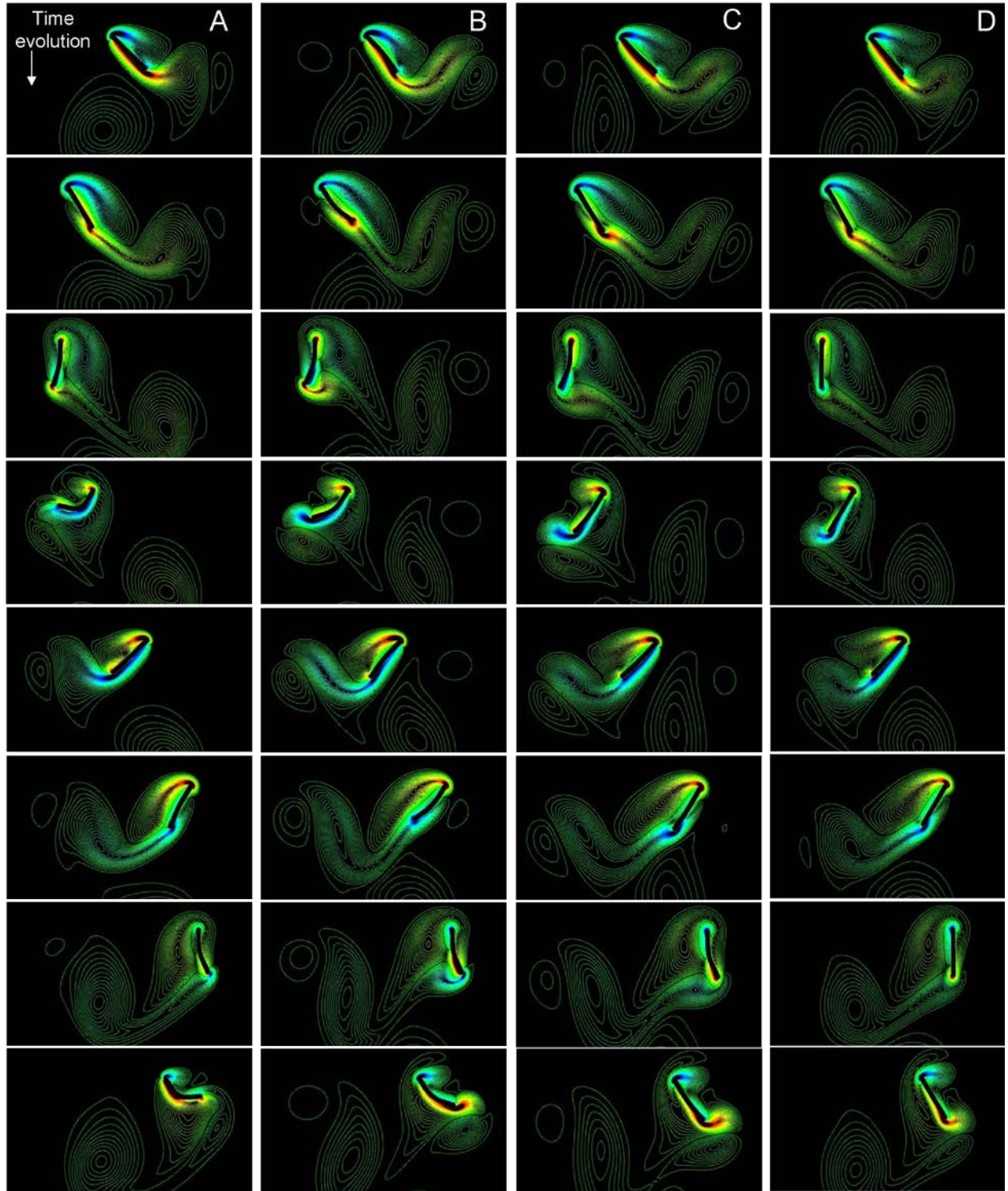


Figure 5: Vorticity contours from DNS at $Re = 75$. Contours range from -10 to 10 with 80 intervals. Columns A-C are flexible profiles with $\omega_f/\omega_n \in \{1/2, 1/3, 1/4\}$, respectively; Column D is the rigid profile. Adapted from Vanella *et al.* (2009).

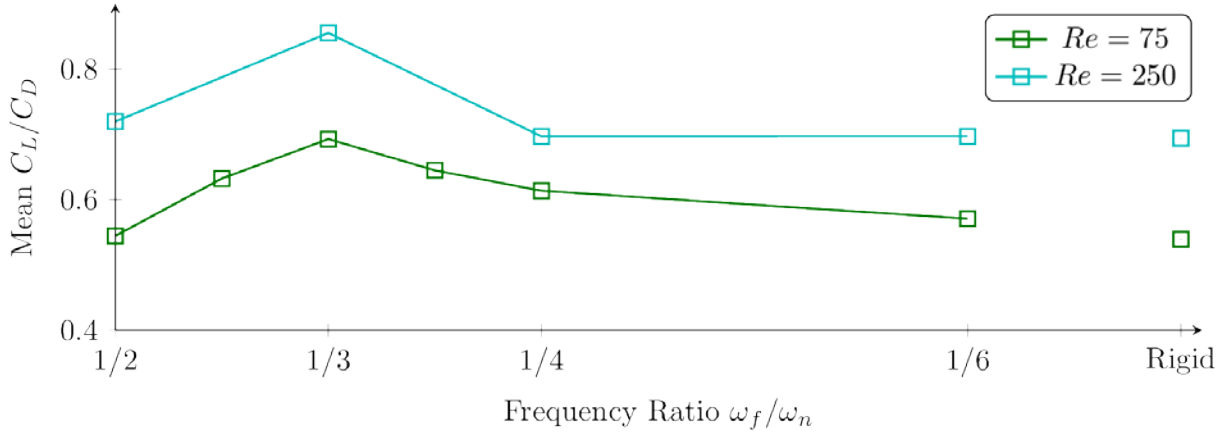


Figure 6: Averaged lift to drag ratio from the two-dimensional DNS calculations for various frequency ratios. Profile thickness is $l/10$.

A summary of the resulting flow fields is depicted in Figure 5 for a range of ω_f / ω_n at Reynolds number $Re = 75$. The vorticity contours reveal the vortex structure interplay with the flexible profile. Similar results were also computed for $Re = 250$ and $Re = 1000$. It is worth noting that for the soft spring case of $\omega_f / \omega_n = 1/2$, the system undergoes extremely large deflections, and the passive link almost undergoes a complete rotation about the joint.

On examining the averaged dimensionless aerodynamic forces acting on the profile, there is an interesting finding. It is observed that for the particular spring value corresponding to $\omega_f / \omega_n = 1/3$, there is a peak in the ratio of lift coefficient and drag coefficient C_L / C_D , as viewed in Figure 6. It is also noted that the flexible profile has an improved efficiency compared to that of the rigid profile.

3.5 Unsteady vortex lattice method in two dimensions

In contrast to the computationally expensive DNS method, vortex methods present a compromise between speed and fidelity. In the unsteady vortex lattice method (UVLM) employed by Preidikman (1998), it is assumed that the flow field is inviscid and the wake can be completely described by point vortices. A body in the flow field is discretized into panels, and the no-penetration condition is applied at the chosen control points along each panel. The discretization used in this method is illustrated in Figure 7.

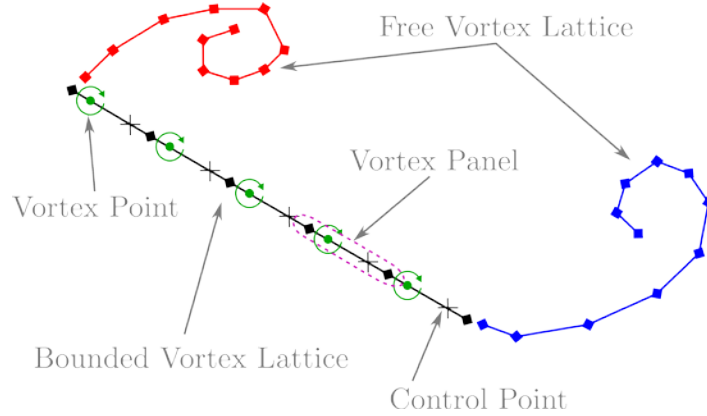


Figure 7: Schematic for the discretization of the Unsteady Vortex Lattice Method.

This method can be applied to a membrane or zero-thickness problems, since assuming the wake to only separate at the edges is suitable. Vortices are convected from the trailing edge after each time step by using the Kutta condition. Similarly, Valdez *et al.* (2006) proposed a method to convect vortices simultaneously from the leading of the profile. Since a zero-thickness profile is used here, the tips are assumed to be the points where the wake separates from the body. Also proposed by Valdez *et al.* (2006), is a reconstruction of the entire velocity and pressure fields from the vortex particle wake. For the results presented here, the original code was authored by Valdez (2008).

Unlike the slower DNS computations, a complete run of 20 periods of hovering motion takes around 10 hours on an eight processor Intel XEON computer. The issue with longer simulations is that with each additional time step, there are two additional vortices whose influence needs to be included. So the number of computations increases at a rate $O(n^2)$, where n is the number of time steps in the integration. This makes short time computations quick in comparison to a DNS study, but long time simulations quickly become impractical. These characteristics make the UVLM simulations attractive from a design perspective since coarse results can be obtained rather quickly.

3.6 POD analysis of the flow fields

3.6.1 Formulation

The proper orthogonal decomposition (POD) goes by many names such as the Karhunen-Loève transform, principal component analysis, or singular systems analysis depending on the discipline. It also can be formulated in a continuous or discrete sense, and used for experimental or computational data. The overarching goal of the POD is to decompose data into hierarchical sets of spatial basis functions, often called mode shapes. Here the velocity fields of the fluid are

decomposed into spatial modes by using the continuous approach. This gives the assumed representation of the flow field the following form

$$\mathbf{u}(\mathbf{x}, t) = \sum_{i=1}^{\infty} \alpha_i(t) \phi_i(\mathbf{x}). \quad (3.4)$$

This can be interpreted from a vibrations perspective as time-dependent coefficients in modal coordinates. The modes $\phi(\mathbf{x})$ are chosen to maximize the projection of the empirical data onto these modes in a L^2 sense. So the problem statement is formulated as in the work of Holmes *et al.* (1996), and further simplifications can be made, since it can be recognized that the modes are a special superposition of the data snapshots. Employing the *method of snapshots* (Sirovich, 1987), the modes ϕ can be approximated as a finite sum over the known data

$$\phi_i(\mathbf{x}) = \sum_{k=1}^M \psi_{ik} \begin{bmatrix} u(\mathbf{x}, t_k) \\ v(\mathbf{x}, t_k) \\ p(\mathbf{x}, t_k) \end{bmatrix}. \quad (3.5)$$

O'Donnell and Helenbrook (2007) demonstrate through a scaling argument that the pressure components can be neglected for incompressible flow in the substitution back into the Fredholm equation. This means that only the velocity field is needed for the computations, while the modes of the pressure field are still computed. The simplified results become an algebraic eigenvalue problem of size M

$$\mathbf{C}\psi = \lambda\psi \quad (3.6)$$

where

$$C_{lk} := \frac{1}{M} \int_{\Omega} \mathbf{u}(\mathbf{x}, t_l) \cdot \mathbf{u}(\mathbf{x}, t_k) dV. \quad (3.7)$$

Since $\mathbf{C} = \mathbf{C}^T$ only the upper or lower triangular part needs to be constructed. So the process to construct the POD set can be described as a sequence of the following steps:

- Generate velocity field data at equal time intervals.
- Construct each element of (3.7) by integrating over the domain.
- Solve the $\mathbb{R}^{M \times M}$ algebraic eigenvalue problem of (3.6) to get the set of eigenvalues λ and the associated eigenvectors ψ .
- Back substitute ψ into (3.5) to get a truncated set of POD eigenfunctions ϕ .

The set of spatial mode shapes ϕ are ranked by using the eigenvalues λ . This gives a quantitative measure to regard the importance of each mode as constructed from the data. For all the examples considered below, 99% of the energy in the snap shots is contained in less than 10 of the leading eigenvalues. This significant roll-off means that one can consider just a few leading terms. A noteworthy side effect of the POD obtained by using the method of snapshots is immediately appreciable; ϕ must be divergence free. Since the mode shapes are a weighted super position of divergence free data, then ϕ must also be divergence free (incompressible). So any use of these modes faithfully preserves the incompressibility of the flow field.

3.6.2 Results

Next, the results obtained from various POD computations are presented. Note that these figures represent the flow field outside of time, and they are the hierarchical structures of the fluid flow. The center joint of the profile moves through the region $(x/l, y/l) = (\pm 1.4, 0)$.

In Figure 8, the vorticity contours of the computed modes are shown for $Re = 75$. The plotted field is the curl of the velocity mode shape, normalized to have the maximal value be one. This makes comparison between modes informative. After examining this figure, it is observed that all of the mode one results contain a large pair of vortices. This represents the downward jet of fluid, and produces lift on the profile. For $\omega_f / \omega_n = 1/3$, this pair of vortices is the most intense as well as closest to the region of the body. Interestingly this corresponds to the most efficient response for the given harmonic input kinematics. It also corresponds to the structural resonance for the kinematics being used. As expected, the scale of the structures decreases as the mode number increases. This follows intuition from vibration mode shapes.

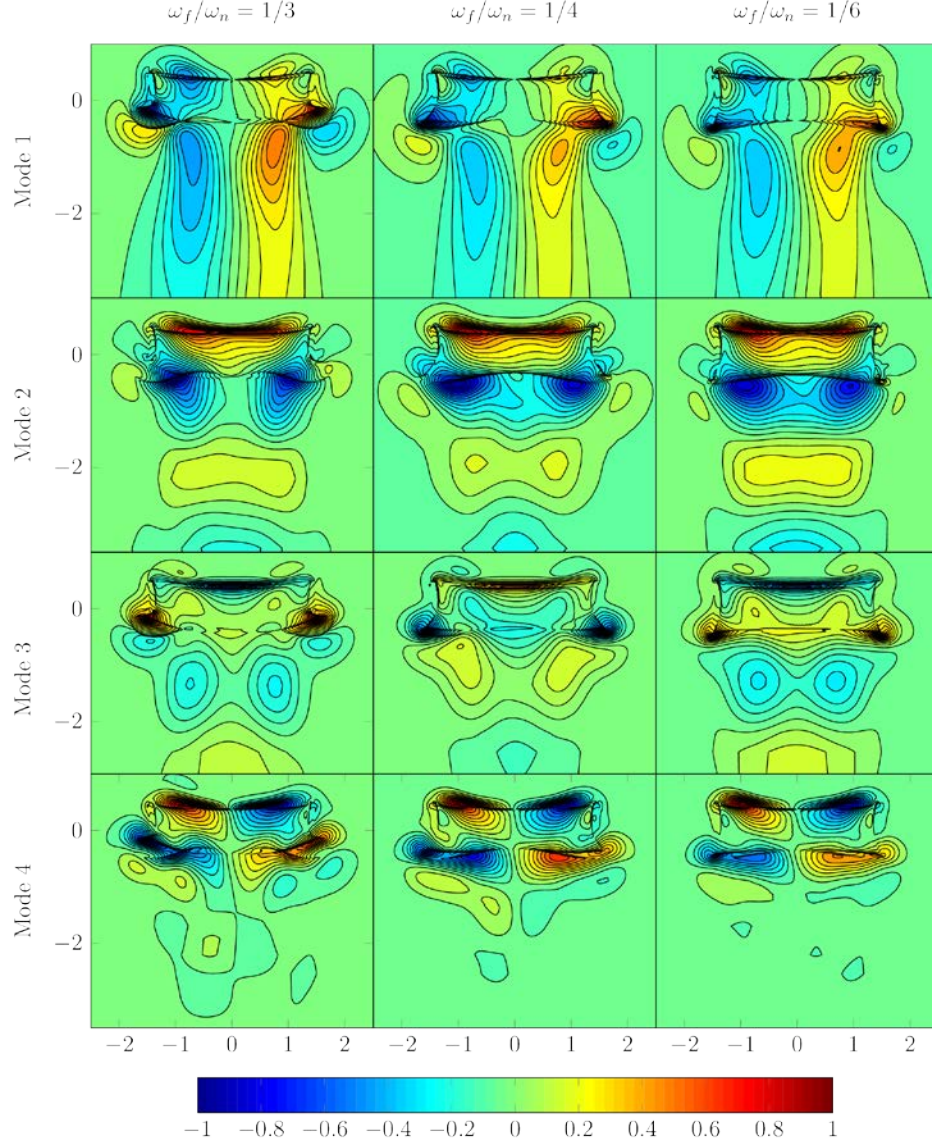


Figure 8: Vorticity contours determined by POD from DNS at $Re = 75$, 10% thickness, and harmonic kinematics. Normalization is $\max_{\mathbf{x}} |\nabla \times \phi_i(\mathbf{x})| = 1$. Horizontal scale is x/l , vertical scale is y/l .

The results obtained for $Re = 250$ are shown in Figure 9. It is interesting to note similar patterns to those obtained for the low Reynolds number configuration; again, mode one components shows a downward jet and mode two shows the end of stroke vortex pair. In this flow regime, the vortices for the spring of intermediate stiffness ($\omega_f / \omega_n \in \{1/3, 1/4\}$) appears to be more spatially regular. An investigation using other kinematics would need to be carried out in order to see how the kinematics affects the regularity of the field.

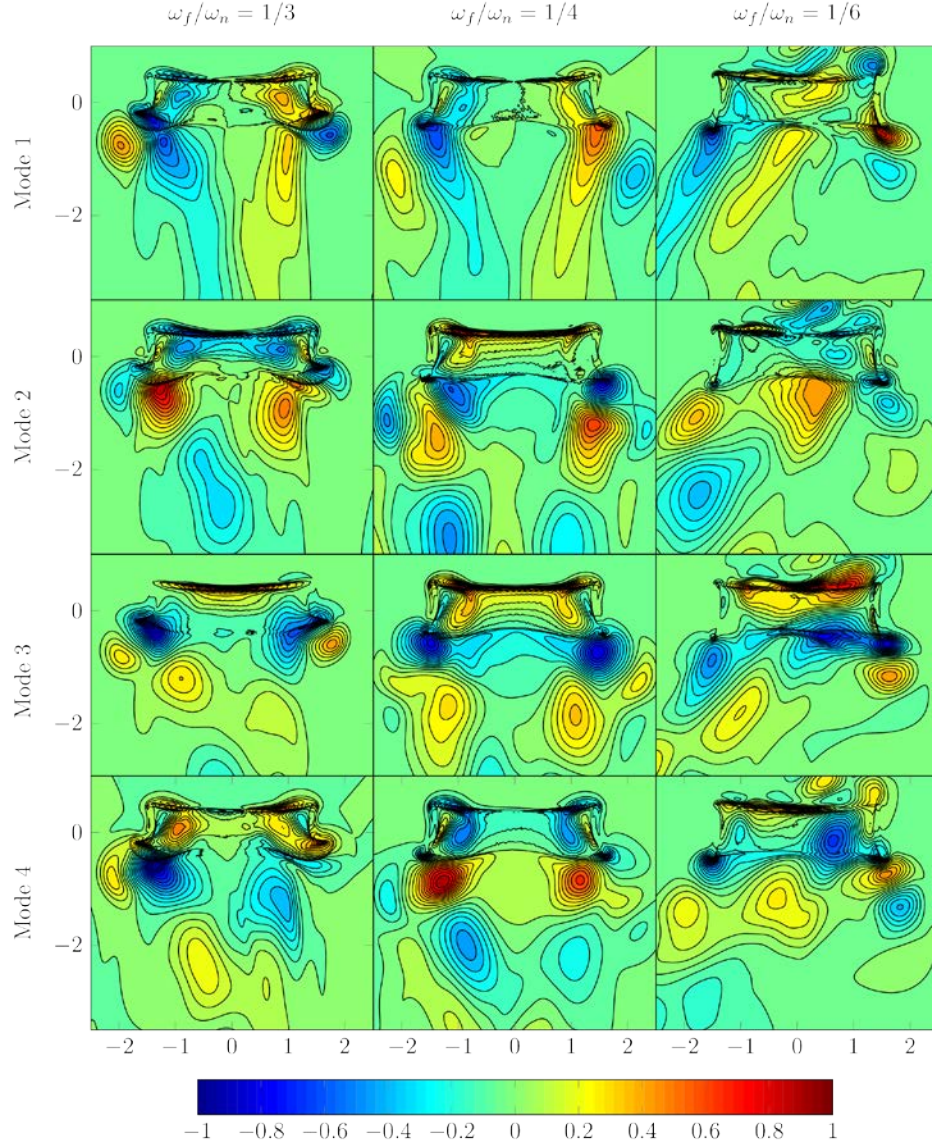


Figure 9: Vorticity contours determined by POD from DNS at $Re = 250$, 10% thickness, and harmonic kinematics. Normalization is $\max_{\mathbf{x}} |\nabla \times \phi_i(\mathbf{x})| = 1$. Horizontal scale is x/l , vertical scale is y/l .

Comparing the mode shapes of DNS fields to the UVLM fields cannot be done with vorticity contours since the UVLM approach is inviscid in nature. Instead the velocity contours must be compared. As discussed later in §3.7, the UVLM velocity modes share similar features to the DNS generated modes.

3.7 Comparing the results from DNS and UVLM studies

The discussion in this section follows from the published work of Fitzgerald *et al.* (2011). The goal is to compare the DNS and UVLM models to see where and how each should be best employed. A DNS simulation is expensive; in fact, it would take several weeks for a full run of 15 periods. By contrast, the UVLM can produce 15 periods of flapping in several hours. The DNS results are expected to be better, since it fully models the physics of interest. However, as shown by Fitzgerald *et al.* (2011) the trends observed in the UVLM simulations for various configurations agree well with those noted in the DNS studies. This provides a hybrid approach to use for system designers: the UVLM simulations can be first used as a low-fidelity prediction tool to find parametric regions of interest, which can be followed by the use of DNS studies to compute more realistic data.

3.7.1 Flow fields

In Figure 10, comparisons among the flow fields obtained through the DNS studies for $Re = 75$, 250 and 1,000 and the UVLM are shown for period 6. The ratio of the forcing frequency to the natural frequency of the system is chosen to be $\omega_f / \omega_n = 1/2$ to show the largest displacements observed. The magnitude of the velocity field is shown, since the vorticity field is unavailable from the UVLM simulations. In these figures, the different vortex structures can be observed and compared as the viscous diffusion in the system is decreased.

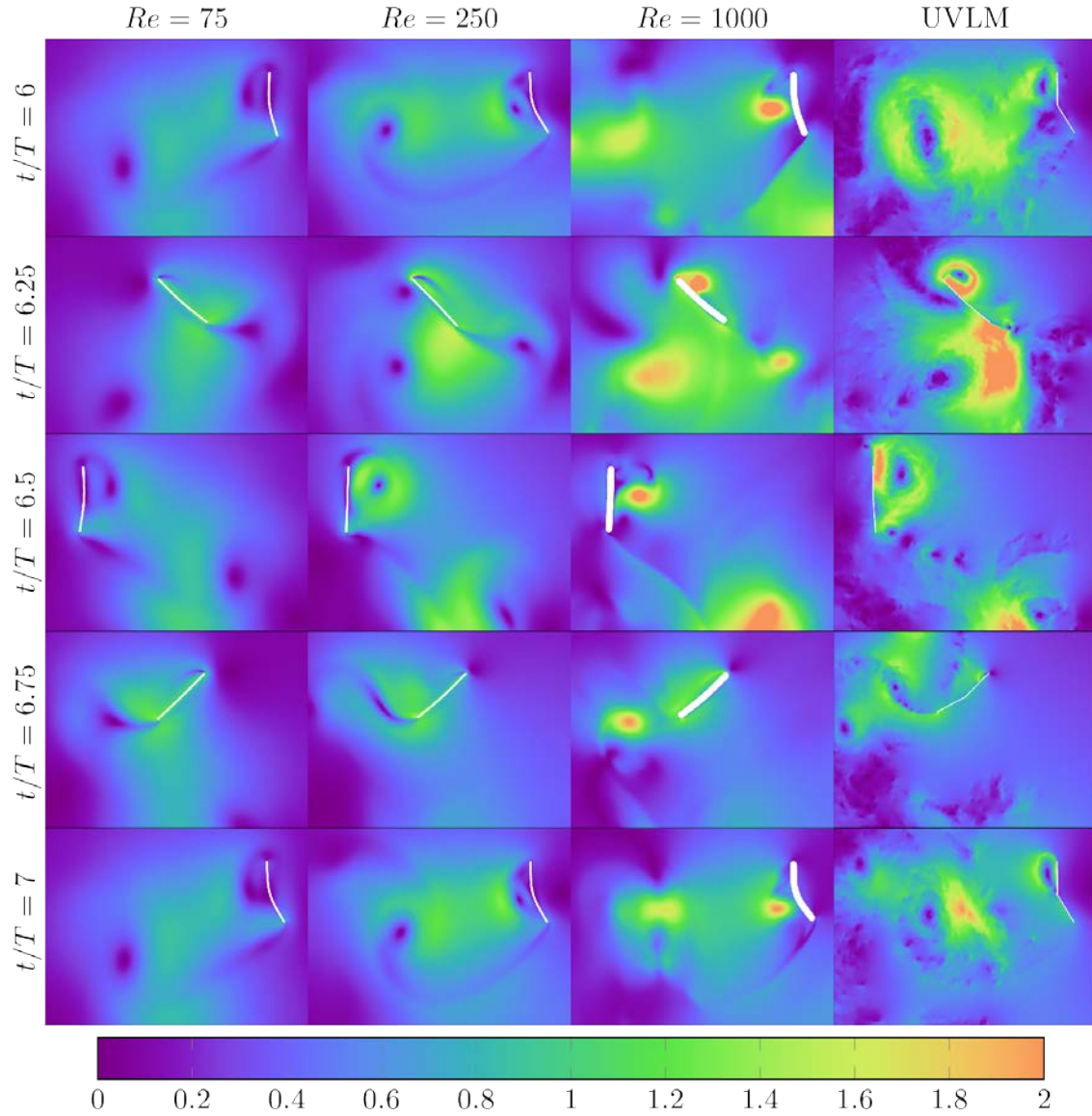


Figure 10: Magnitude of the velocity fields from periods 6--7 for $\omega_f / \omega_n = 1/2$, DNS at

$Re \in \{75, 250, 1000\}$, and UVLM. The velocity field is normalized as $|\mathbf{u}|_2 / u_{\text{ref}}$.

For $Re = 75$, the flow field snapshots throughout periods 6 and 9 are nearly identical, resulting in the periodicity of the flow field. This matches with the calculations of the correlation dimension, which suggests that a periodic orbit is produced in the low Reynolds number case. When $Re = 250$, the snapshots are also very similar between periods 6 and 9. However, as the correlation dimension indicates, an exact periodic solution is not seen. There are small enough differences in the flow fields to cause small disturbances to what is nearly a periodic orbit. At $Re = 1000$, with relatively low viscous diffusion, the flow field no longer appears to be periodic. However, the same kind of vortex structures can be identified as in the low Reynolds number

cases, such as the leading and trailing edge vortices. As expected, the intensity of these vortex structures increases, since they are proportional to the magnitude of the velocity. The non-periodicity of the flow field is a consequence of vortex interactions that were not dominant in the low Reynolds numbers cases.

A sample of the velocity POD mode shapes obtained from the DNS and UVLM studies is shown in Figure 11. Here, the downward jet appears in the vertical velocity. Around the body, traces of the end of stroke vortices can be noted. The UVLM contains no viscous dissipation which is why the fluid structures do not dissipate in time. The results show that the UVLM POD is still able to nicely quantify the flow field in terms of the dominant structures.

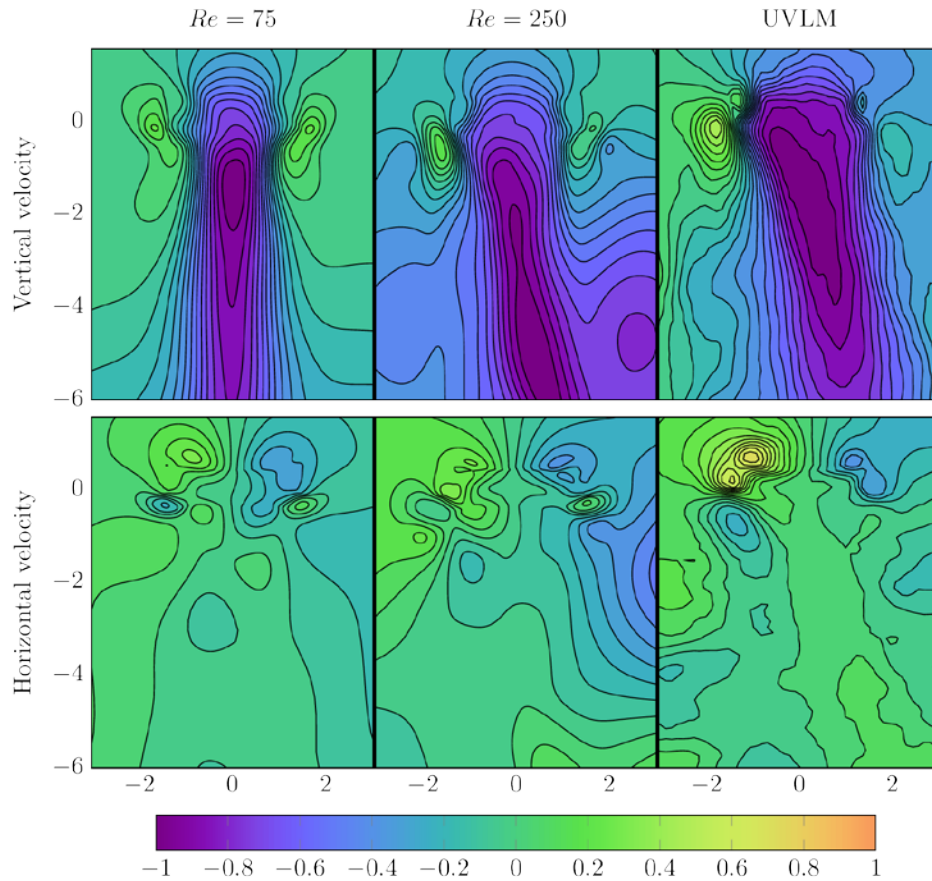


Figure 11: Comparisons of Mode 1 of POD velocity contours from DNS and UVLM data for $\omega_f / \omega_n = 1/3$ with harmonic kinematics. The fields are normalized by $\max_{\mathbf{x}} |\phi_i(\mathbf{x})|_2 / u_{\text{ref}} = 1$.

Horizontal scale is x/l , vertical scale is y/l .

3.7.2 Aerodynamic loads

The aerodynamic forces of interest here are the lift force and the drag. The lift is defined as the vertical force; or the force that would keep a hovering system from falling. The dimensionless lift is

$$C_L = \frac{Q_y}{\frac{1}{2} \rho_{\text{fluid}} u_{\text{ref}} l^2} \quad (3.8)$$

where Q_y is the vertical force. Since the vertical motion of the joint is zero, the drag is taken to be the horizontal force that opposes the horizontal translation. The dimensionless drag is

$$C_D = -\text{sgn}(\dot{x}) \frac{Q_x}{\frac{1}{2} \rho_{\text{fluid}} u_{\text{ref}} l^2} \quad (3.9)$$

where Q_x is the horizontal force. Observing the time series obtained through DNS at $Re = 1000$ and the UVLM shows that the signals initially match quite well, as seen in the first period and a half in Figure 12. As the simulation evolves however, the solutions appear to diverge, but still follow similar trends. The loads from the UVLM successfully capture the dominant characteristics, with similar peaks and valleys in $C_L(t)$ corresponding to the mid-stroke and stroke reversals, respectively. In both the lift and drag coefficients the UVLM results appears to follow the same pattern of over-estimating the highs and lows. This suggests that the simulation of a transient maneuver, such as clap and fling (Weis-Fogh, 1973), and averaged long-term dynamics may be reasonably predicted by using UVLM simulations. To explore long-term dynamics, a statistical approach is needed.

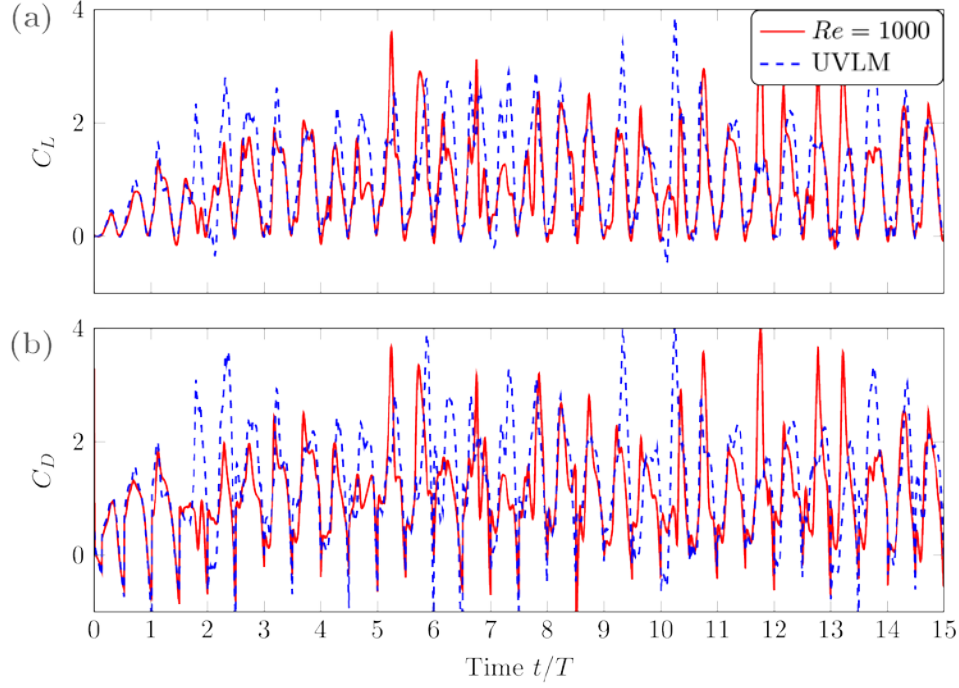


Figure 12: Time series of the dimensionless loads of the hovering profile from DNS at $Re = 1000$ in red and UVLM in blue for the frequency ratio $\omega_f / \omega_n = 1/3$.

The time histories have been collapsed to a single period by phase-averaging in Figure 13. The data from periods 5 through 15 are averaged by using the hovering period T as the reference clock. This range of time is used since the hovering kinematics has reached the full amplitude, and the startup transients in the fluid should have died down. At the stroke reversal, when $t/T \in \{0, 1/2\}$, there is a jump in C_D that is not fully captured by the UVLM simulations. A possible reason for the discrepancy could be that the vortex interaction during this event is influenced more by viscosity than at other points of the cycle. For softer spring values; that is, $\omega_f / \omega_n \in \{1/2, 1/3, 1/4\}$, the curves generally are in better agreement. This is particularly visible in the case of the lift. The prediction is worst for the rigid case.

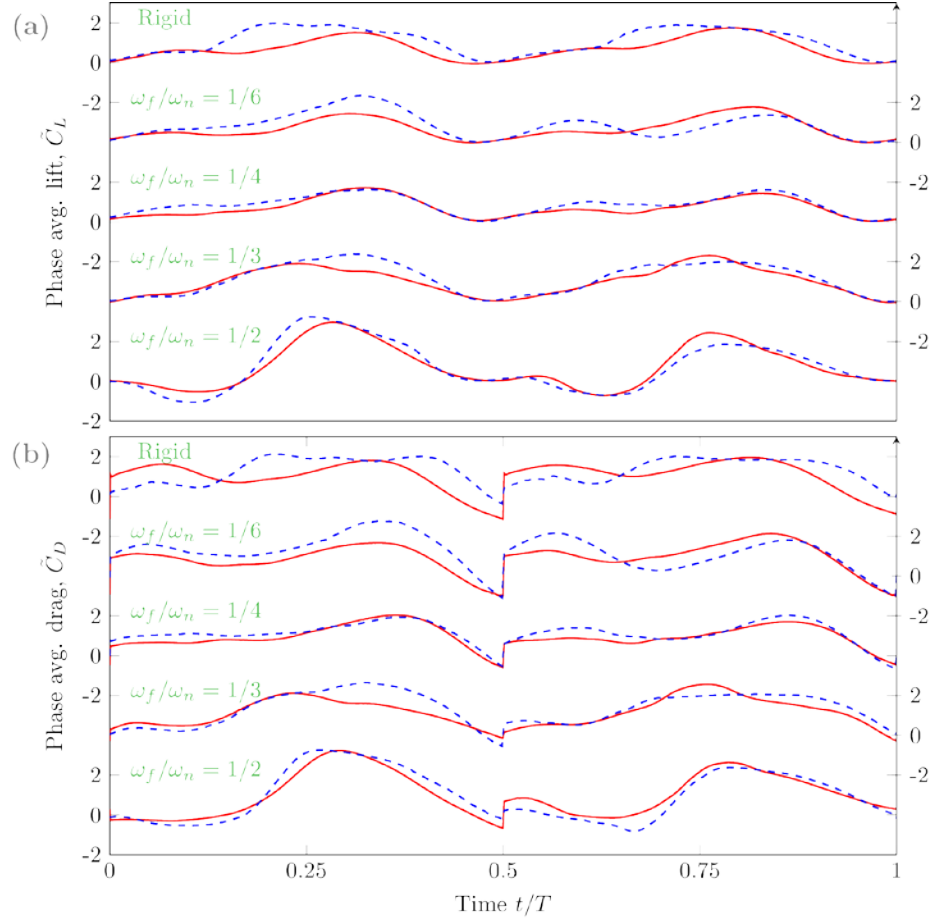


Figure 13: Phase averaged forces of the hovering profile from DNS at $Re = 1000$ in red and UVLM in blue for various frequency ratios. (a) Lift coefficient and (b) drag coefficient. Adapted from Fitzgerald *et al.* (2011).

The quantitative comparison of which UVLM curve best matches the corresponding DNS curve requires another definition. The error measure assumed here is a scaled L^2 -norm. This is a point-wise check to see how far off the UVLM is at every point in time. This does not account for phase lag or lead between the models. For the drag force, it is written as

$$\text{error}(\tilde{C}_D) := \frac{\left(\int_0^T (\tilde{C}_D^{\text{DNS}}(\tau) - \tilde{C}_D^{\text{UVLM}}(\tau))^2 d\tau \right)^{1/2}}{\max \tilde{C}_D^{\text{DNS}} - \min \tilde{C}_D^{\text{DNS}}} \quad (3.10)$$

with the same form being used for the lift coefficient \tilde{C}_L . The numerical values are compiled in Table 1. The differences appear to be smaller for the more compliant structures, indicating that the UVLM model would be of better use in highly flexible configurations where the structural

Table 1: Relative error values of the phase-averaged loads between the $Re = 1000$ DNS and UVLM results for a range of stiffnesses.

Rel. Error	Frequency Ratio ω_f / ω_n				
	1 / 2	1 / 3	1 / 4	1 / 6	Rigid
\tilde{C}_D	9.9%	15.9%	10.0%	19.6%	24.7%
\tilde{C}_L	9.6%	13.4%	13.6%	25.6%	28.8%

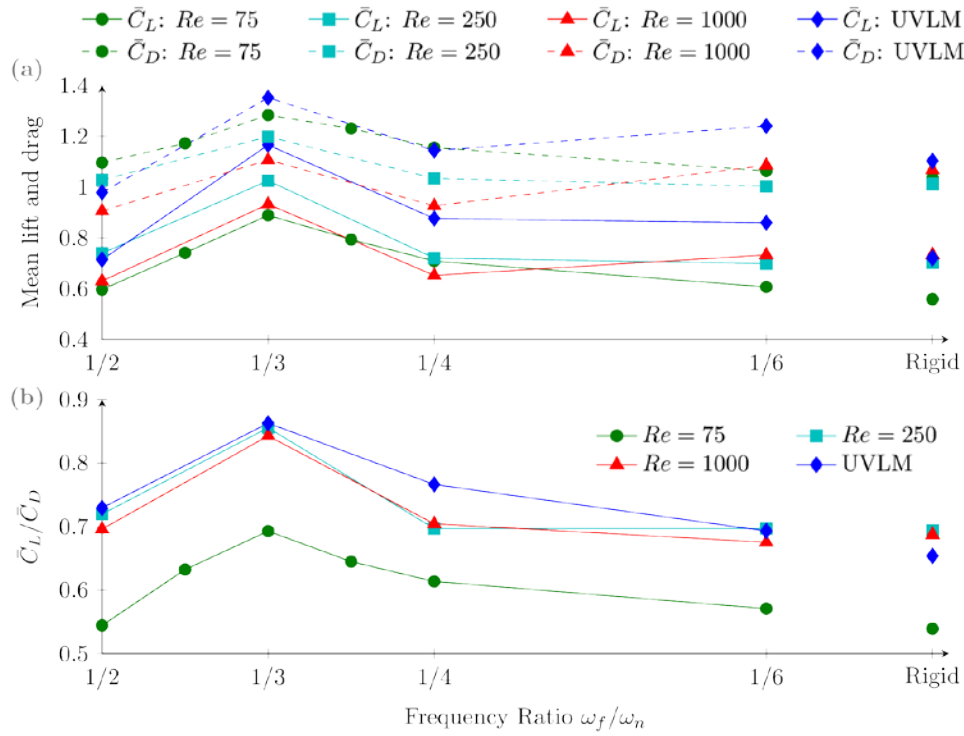


Figure 14: Comparisons of time averaged dimensionless lift and drag coefficients from the UVLM and DNS at various Re . (a) Mean lift and drag coefficients, (b) the ratio of mean lift to mean drag. Adapted from Fitzgerald *et al.* (2011).

dynamics outweigh the fluid contributions. Overall, the predictions are likely acceptable in engineering design since the compliant configuration have errors that are less than 20%.

Taking the overall time-average of the loads provides an even better use of the UVLM results. As shown in Figure 13, the time averaged loads \bar{C}_L and \bar{C}_D trend together. The UVLM simulations overestimate the lift and the drag, but since it is nearly by the same 15% the ratio of the quantities match the DNS results quite well. Keeping the modeling and kinematic

assumptions in mind, the results indicate that moderate flexibility improves the aerodynamic performance.

The results of Figure 13 indicate that the UVLM study is adequate for quasi-steady prediction. Furthermore, the results of Figure 14b demonstrate that the UVLM is quite suitable for a designer to predict gross quantities and trends. The trends with respect to the spring parameter are the most significant, since it points to the UVLM study being suitable for use in an optimization setting. As mentioned earlier, a designer could adopt a hybrid approach and use the UVLM simulations in an optimizer to find parametric regions of interest and follow this up with detailed investigations of these regions with DNS studies.

4 Three-Dimensional Modeling

4.1 Introduction

A survey of the technology to extend the flapping work into 3D problems quickly reveals that the modeling of the structure is less well understood than the modeling of the fluid. The Navier-Stokes equation for an incompressible Newtonian fluid is an extremely versatile and well-understood model. Even a vortex lattice method in 3D is well suited for certain problems. The model for a body or structure, by contrast, is still an open item. Not merely the geometry is variable, but the structure itself and how to model its behavior is open. Recent work on modeling the flapping wing-fluid system have either included rigid wings or highly simplified models. In the work of Pai *et al.* (2009), a body described by nonlinear structural elements interacts with a quasi-steady fluid. In an experimental study, Zhao *et al.* (2010) measured the forces on a flapping wing made with Mylar material. The synthesis of natural fliers to the construction of micro aerial vehicles is also a topic of open interest.

The goal of this section is to present a structural model that is modular enough to be adapted to a variety of geometry and material properties, and can be designed for use in concert with a large-scale fluid simulation. The finite element method (FEM) provides a nice foundation to base the model since there is extensive literature on many aspects of its use. The FEM is also adaptable to nearly any geometry and has the potential to be generalized for a wide range of material systems.

For the immersed boundary methods employed in the available large-scale fluid solver, a body with finite thickness is required. It was this same requirement that necessitated the placement of a surface around the structural elements in the 2D work of the previous section. Several fluid grid points must be considered inside the solid body for the pressure to be resolved properly. Therefore, the body description selected was a solid body, and not a plate or shell. This provides a natural thickness to the model, and allows for future cases with highly detailed surface geometry such as a computed tomography scan of an insect wing. A solid element also has the benefit that one can directly employ many different material laws from continuum mechanics.

4.2 Experiments

The bio-inspired design of flapping vehicles draws heavily from the work of both engineers and biologists. Among the various interesting aspects of insect, the wing is one of them. Largely thought to be a passively flexible structure, the details of the structure of the wing have long been an area of interest. Comstock (1918) has illustrated a life's body of work, which includes cataloging and defining of the various characteristics of insect wing morphology. His naming conventions of the venation are still in common use by biologists today. Following these footsteps, the efforts of Wootton (1992) further built on the biological map of insect wings.

Early engineering-type studies to model the wing include the efforts of Combes and Daniel (2003a, 2003b, 2003c) and the PhD dissertation of Wootton's student (Herbert, 2001). Both groups come from a biology background, and they make claims that the flapping frequency observed is the fundamental frequency of the structure of the wing. This notation that an insect flaps at linear resonance has only recently been challenged. Computationally, this does not agree with the results shown in §3.7.2 since those models predict that efficiency decreases as linear resonance is approached (Fitzgerald *et al.*, 2011; Vanella *et al.*, 2009).

Experimentally, Sims (2010) showed that the first natural frequency of a hawkmoth wing is around twice that of the flapping frequency. The spectral information was measured via a scanning laser vibrometer from wings recently removed from living hawkmoths. The tests were repeated for several specimens in air and in a vacuum chamber, and the measured first natural frequency is around twice the flapping frequency. Kang *et al.* (2011) made several scaling arguments that predict the optimal natural frequency to be around 1/3 to 1/2 of the flapping frequency. This recent work indicates that not only could older assumption be wrong, but there is a tremendous opportunity to exploit nonlinear effects.

The setup to measure the spectral response of a living insect is outlined in Figure 15. A living insect is anesthetized by exposure to a large amount of Flynap² and then placed in a fixture molded out of modeler's clay. The forewing is fixed in place near the root with more clay and pins. The wing is acoustically excited by a JBL ASB1728 loudspeaker. This subwoofer is rated to 4000 W of continuous pink noise, and has high fidelity down to 20 Hz. A pseudo-random signal is output from the Polytec PSV-400 vibrometer controller to a Crown MA-9000i power amplifier connected to the loudspeaker.

The choice of the *Manduca sexta* was made due to several key factors. It has been widely studied by biologist and found to be rather uniform in its body and flight characteristics across individuals. The insect wing is relatively large and opaque. This means that it can be measured by standard vibrometer equipment already available in the Vibrations Laboratory. This insect species can be easily procured and grown from larvae purchased from biology supply companies. During the design of the experiment, it was thought that the fundamental frequency of these insects was near 25 Hz (Combes and Daniel, 2003a, 2003b, 2003c). This drove the interest in the use of a speaker with good low frequency fidelity.

² Flynap is a general anesthetic designed for *Musca domestica*. It is composed of 50% Triethylamine, 25% Ethanol, and 25% Fragrance, per the Material Safety Data Sheet <http://www.carolina.com/pdf/msds/FLYNAP.pdf>

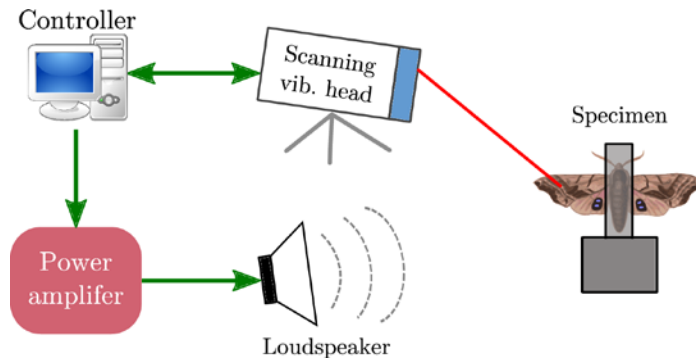


Figure 15: Schematic depicting the use of a scanning laser vibrometer to characterize the spectral response of a living insect wing using non-contact excitation.

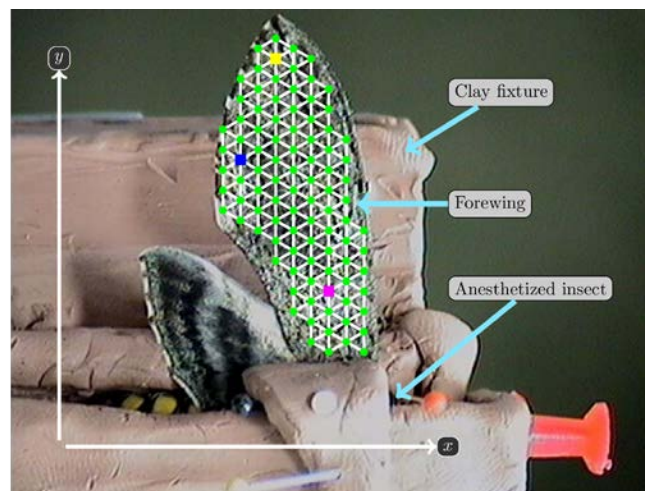


Figure 16: Mesh of the scanning laser vibrometer on a living *Manduca sexta* forewing. The color markers indicate locations of signal points in Figure 17. Note that $+x$ is in the vertical direction.

The scanning laser vibrometer is then setup to measure the response of a set of points on the surface of the wing. This mesh is shown in Figure 16. The laser vibrometer is placed such that the wing is centered and parallel in the viewfinder. The scanning is performed sequentially, and the frequency information from each point is stored as complex Fast Fourier Transform (FFT) data. Since the total number of FFT data points per mesh point is limited by the software, there is a trade-off of spectral resolution when selecting the frequency range of interest. By choosing the maximum number of FFT data points at 6400, and selecting the frequency range of interest to be 0-1000 Hz, a working resolution around 0.25 Hz was obtained.

By examining the FFT data from several key points around the wing, the first natural frequency of the wing can be easily located. In Figure 17, the normalized FFT results are shown for points near the root, the tip, and the trailing edge. The measurements made at these spatial points indicate that the first natural frequency of the wing specimen is around 77 Hz. Locating the

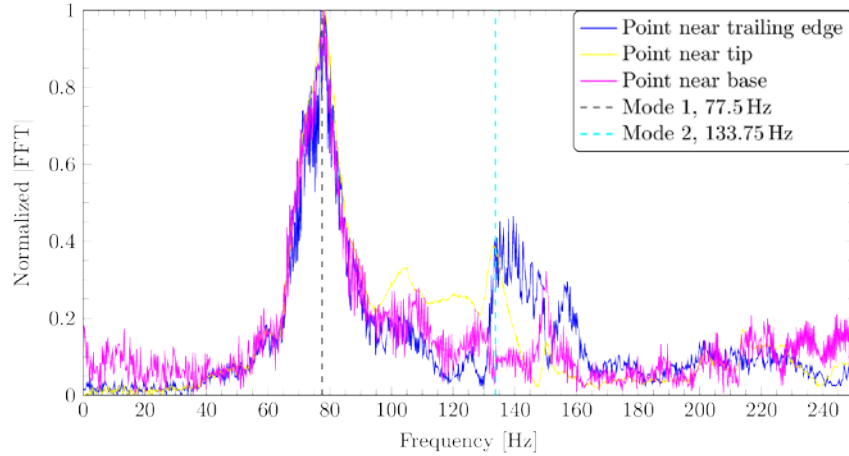


Figure 17: Normalized magnitude of the FFT of the velocity data determined from the laser vibrometer at various points on the forewing of a *Manduca sexta*. The color points are indicated on Figure 16.

second natural frequency is a bit more challenging, since the response of the wing appears is found to be rather complicated.

By searching through the visualizations of the stitched mode shapes on the PSV-400 system, it is found that around 134 Hz, there is another mode shape. The noise floor is too high at the higher frequencies to be confident in locating other natural frequencies and associated mode shapes. This problem is inherent in the non-contact excitation provided by using a speaker. The natural frequencies reported here agree well with those of Sims (2010), who used an amputated wing directly mounted to a shaker and could therefore work with much higher frequencies and amplitudes of excitation. The novelty of the speaker experiments is that the insect and wing were alive during and after the entire measurement process. The wing measured here has not been altered by death, atrophy, or temperature. Sims had to measure the severed wings within several hours to ensure that they had not changed significantly, whereas in the current study, the researchers had around 30 minutes, the window in which the insect remained asleep.

Reconstructions of the mode shapes associated with the first two natural frequencies are shown in Figure 18. Here, the data was extracted from the proprietary Polytec data file, and plotted in Matlab. The x and y coordinates are scaled by the span of the wing l , and the vertical displacement of the mesh is scaled such that the maximum is $l/8$. The choice of vertical scaling is arbitrary since the representation is for a mode shape, and the choice of $l/8$ was merely made for visualization purposes. The first mode, which is shown in Figure 18a, appears to correspond to spanwise bending. The second mode, which is shown in Figure 18b, appears to be a combination of chordwise bending and some bending near the tip. A possible use for this type of detailed information is in the construction of wing models tailored to perform like a *Manduca*

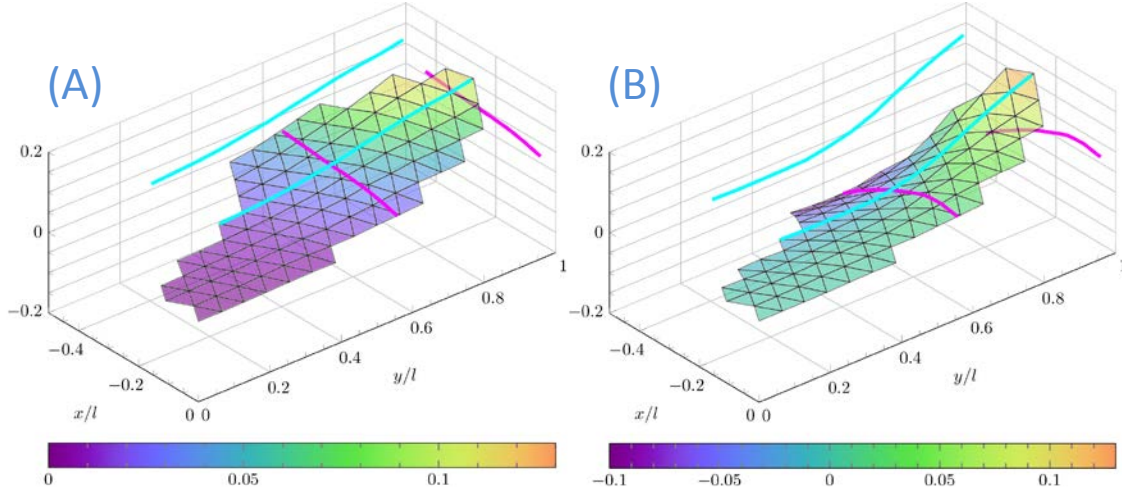


Figure 18: Experimentally determined modes of a living *Manduca sexta* forewing. The x and y coordinates are scaled by the wing span, z is scaled such that the $\max z/l = 1/8$ for visualization. (A) Mode 1 at 77.5 Hz. (B) Mode 2 at 133.75 Hz.

sexta. The distribution of material properties could be designed such that the first two natural frequencies of the model resemble the experimental results.

4.3 Implementation using geometrically exact finite elements

The goal of the tools constructed here are to explore fluid-structure interaction problems, like flapping wings. Solid finite elements are used since the supporting theory and technology is widely known. They provide a foundation to build a framework that many different types of structures, wings, material models, and so on, can be tested. The implementation is general enough to handle structural elements as well, and their integration is a possible avenue for future work. Solid models were chosen since they provide finite thickness, fundamentally have the fewest assumptions, and they can be widely adapted for a variety of continuum-mechanics based response models. The relative cost of using solid elements in a large-scale CFD simulation is not low.

The implementation technology employed here is largely based on Hughes (2000) for the assembly and shape functions and Belytschko *et al.* (2000) for dealing with nonlinear models. Mesh generation is designed around the open-source software Gmsh (Geuzaine and Remacle, 2009). The elements implemented are isoparametric quadratic hexahedra for the volume of the body. These 27-node displacement based elements were selected since they do not suffer from locking like linear elements. Surface elements used for the FSI and other loading are 9 node quadrilaterals. Each quadrilateral is coincident to a single face of a corresponding hexahedron.

The implementation contains both Kirchhoff and Biot material models for isotropic properties. The implementation of the Biot material was selected since it represents a generalization of the

engineering stress-strain law to finite deformations with arbitrary rigid body motions. This method was selected since it provides a pattern for future code development for problems with anisotropic materials.

4.3.1 Equations of motion

The description of motion implemented is a weak-form of momentum conservation often called the Total Lagrangian formulation. It is a Lagrangian method where everything is expressed in terms of the reference configuration. In the usual finite element way, the virtual work of the body is expressed as

$$\delta W_{\text{int}} - \delta W_{\text{ext}} = 0 . \quad (4.1)$$

The virtual internal work can be expressed in terms of any work-conjugate pair. The simplest pair to work is (\mathbf{E}, \mathbf{S}) , which in Voigt notation takes the form

$$\delta W_{\text{int}} = \int_{\Omega_0} \{\delta E\}^T \{S\} dV_0 = \sum_{e=1}^{n_{el}} \delta W_{\text{int}}^e . \quad (4.2)$$

The external work can be viewed as the sum of work due to body forces, such as acceleration and gravity, and surface tractions.

$$\delta W_{\text{ext}} = \delta W_{\ddot{\mathbf{u}}} + \delta W_{\mathbf{f}_{\text{ext}}} \quad (4.3)$$

The surface forces will be treated in §4.3.2. The acceleration term can be written as

$$\delta W_{\ddot{\mathbf{u}}} = \int_{\Omega_0} \delta \mathbf{u} \cdot (-\ddot{\mathbf{u}} \rho_0) dV_0 . \quad (4.4)$$

By using the usual finite element shape function approximations

$$\mathbf{u} = \mathbf{N} \mathbf{q} \quad (4.5)$$

one obtains the consistent mass matrix.

$$\begin{aligned} \delta W_{\ddot{\mathbf{u}}} &= \int_{\Omega_0} \delta \mathbf{q}^T \mathbf{N}^T (-\mathbf{N} \ddot{\mathbf{q}} \rho_0) dV_0 = -\delta \mathbf{q}^T \int_{\Omega_0} \rho_0 \mathbf{N}^T \mathbf{N} dV_0 \ddot{\mathbf{q}} \\ \mathbf{M} &= \int_{\Omega_0} \rho_0 \mathbf{N}^T \mathbf{N} dV_0 \end{aligned} \quad (4.6)$$

Notable features of this matrix are that it is symmetric, and constant. The symmetry allows for computational efficiency in terms of storage and inversion. The fact that it is constant means it

only needs to be built once. In explicit dynamic algorithms, it needs to only be decomposed once as well. This formulation is still consistent with large motions, and no implied assumptions about the body have been made. The principle of the conservation of mass can be used to show that this constant mass matrix in the Total Lagrangian formulation is equivalent to the deformation dependent mass matrix by other formulations like the updated Lagrangian form (Belytschko et al., 2000).

After combining (4.2) and (4.6) into (4.1), the result is

$$0 = \delta \mathbf{q}^T (\mathbf{f}_{\text{int}} + \mathbf{M}\ddot{\mathbf{q}} - \mathbf{f}_{\text{ext}}).$$

After inclusion of linear damping, this can be recast as the semi-discrete equation of motion

$$\mathbf{M}\ddot{\mathbf{q}}(t) + \mathbf{D}\dot{\mathbf{q}}(t) + \mathbf{f}_{\text{int}}(\mathbf{q}, t) = \mathbf{f}_{\text{ext}}(\mathbf{q}, t) \quad (4.7)$$

The calculation of \mathbf{f}_{int} is determined by how the selected material model is used to compute the second Piola-Kirchhoff stress \mathbf{S} . Essential boundary conditions have not yet been applied to this equation and these boundary conditions are needed, along with initial conditions, to fully pose the problem.

4.3.2 Application of essential boundary conditions

The degrees of freedom (DOF) of the entire body are ordered during the preprocessing of the mesh to place the restrained components at the end of the global list. Thus if \mathbf{q} are the DOF for the entire body, then, this list is partitioned as

$$\mathbf{q} = \begin{bmatrix} \bar{\mathbf{q}} \\ \mathbf{v} \end{bmatrix} \quad (4.8)$$

where the $\bar{\mathbf{q}}$ are the unrestrained DOF, and \mathbf{v} are the DOF that have some essential boundary condition applied to them. Here, $\mathbf{v}(t)$ will be fully defined \mathcal{C}^2 -functions of time that prescribe the motion of points on the body. This permits the direct partitioning of the mass and damping matrices in (4.7).

$$\begin{bmatrix} \bar{\mathbf{M}} & \mathbf{M}_v \\ \mathbf{M}_v & \mathbf{M}_{vv} \end{bmatrix} \begin{bmatrix} \ddot{\bar{\mathbf{q}}} \\ \ddot{\mathbf{v}} \end{bmatrix} + \begin{bmatrix} \bar{\mathbf{D}} & \mathbf{D}_v \\ \mathbf{D}_v & \mathbf{D}_{vv} \end{bmatrix} \begin{bmatrix} \dot{\bar{\mathbf{q}}} \\ \dot{\mathbf{v}} \end{bmatrix} + \begin{bmatrix} \bar{\mathbf{f}}_{\text{int}}(\mathbf{q}, t) \\ \mathbf{f}_{\text{int}}^v(\mathbf{q}, t) \end{bmatrix} = \begin{bmatrix} \bar{\mathbf{f}}_{\text{ext}}(\mathbf{q}, t) \\ \mathbf{f}_{\text{ext}}^v(\mathbf{q}, t) \end{bmatrix} \quad (4.9)$$

Extracting only the top equation for the unconstrained DOF gives the equation of motion with boundary conditions applied; that is,

$$\begin{aligned}\bar{\mathbf{M}}\ddot{\bar{\mathbf{q}}}(t) + \bar{\mathbf{D}}\dot{\bar{\mathbf{q}}}(t) + \bar{\mathbf{f}}_{\text{int}}(\mathbf{q}, t) &= \mathbf{h}(\mathbf{q}, t) \\ \mathbf{h}(\mathbf{q}, t) &:= \bar{\mathbf{f}}_{\text{ext}}(\mathbf{q}, t) - \mathbf{M}_v \ddot{\mathbf{v}}(t) - \mathbf{D}_v \dot{\mathbf{v}}(t)\end{aligned}\tag{4.10}$$

Here the over bars are used to emphasize that these DOF are the free DOF, and the internal and external forces do depend on all the DOF. During the linearization of $\bar{\mathbf{f}}_{\text{int}}$ no additional matrix-partition terms need to be included in \mathbf{h} since their contributions are already present in $\bar{\mathbf{f}}_{\text{int}}(\mathbf{q}, t)$.

4.4 Fluid-structure interactions

4.4.1 Overview

There are many varieties of partitioned methods based on a prediction-correction model. The methods differ in what is used for the prediction, and if the correction is used repeatedly or staggered in time. The method implemented here, as outlined in Figure 19, is sub-iterated until convergence of the entire system's equilibrium is achieved. The fluid solver is based on same explicit fractional step method used, but implemented inside the FLASH framework (ASC Flash Center, 2012; Daley *et al.*, 2012). The large scale high performance computing (HPC) framework is designed to tackle extremely large problem domains on finite-difference grids. In FLASH, one can use either uniform gridding techniques or adaptive mesh refinement (AMR) based on the PARAMESH library (MacNeice *et al.*, 2000).

Each time step is started by predicting the states of the structure, and computing the position, velocity, and acceleration fields of the body's wet surface. Then the fluid velocity field \mathbf{u}^* is

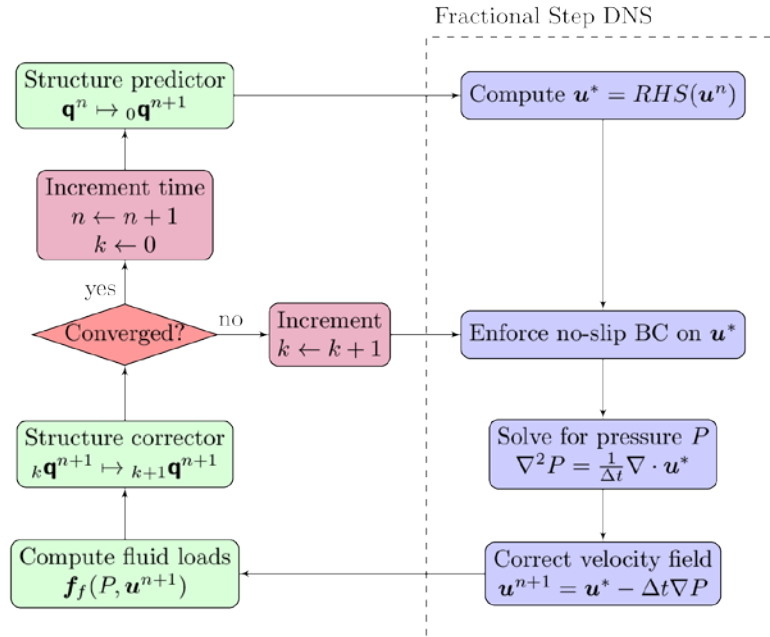


Figure 19: Procedure diagram for the partitioned FSI algorithm.

computed. In the usual manner of fractional step methods, this field is not divergence free. The surface kinematics of the body are then applied to the fluid grid points around the body in a Lagrangian fashion as implemented by Vanella (2010). The calculation of the pressure P presents the most expensive step in the calculation. This elliptical problem, often referred to as the *Poisson problem*, is discretized to become a set of simultaneous linear equations. The efficient calculation of the pressure represents one of the largest hurdles to large scale solutions (Daley *et al.*, 2012). Once the pressure gradient is computed, the corrected (or end-of-step) velocity $\mathbf{u}^{(n+1)}$ is calculated and stored. The velocity and pressure information are then used to compute the surface forces on the body. A corrector procedure then computes an updated estimate of the states of the body. If the states have not changed within some tolerance, then the velocity field of the immersed boundary conditions is recomputed and the cycle repeats. Once the convergence criterion has been satisfied, time is incremented and the outer loop begins again with a prediction of the structure using the previous fluid load.

The implementation issues of the predictor-corrector method used here are mostly surrounding the treatment of the body, since the coding for the fluid model was already in place. This entails both the time integration of the body as well as the construction of the forcing terms as boundary conditions on each partitioned field. Inside the FLASH architecture there is an entire unit of the code dedicated to Lagrangian particle tracking known as PARTICLES. The previous uses of these particles range from physics simulations, to convecting massless particles for event tracing. For the FSI implementation considered here, they will serve as the method of communication between the fluid domain and the structural domain.

4.4.2 Imposition of boundary conditions

Inside the FLASH code, the PARTICLES unit is a well apportioned framework for working with Lagrangian points distributed across the Eulerian domain. The distribution of the particles on the HPC cluster is performed by FLASH. The immersed boundary unit called ImBound uses the information of each particle to enforce the no-slip condition. The use of PARTICLES then is to cover the body's surface with particles whose kinematics is prescribed by the surface of the body. These particle points are used for both parts of the communication of boundary conditions: forcing the fluid and forcing the body.

In Figure 20A, a small collection of particles inside the fixed fluid grid is shown. These particles each represent a small patch of the surface area on the surface of a body (Figure 20B). It is the information of the particles that connects the fluid and structural domains. Each patch of surface must be near the same size as the fluid grid spacing. Therefore the spacing of particles is determined by the fluid grid since for most problems the fluid mesh will be much finer than the body's mesh. This permits the meshing of the structure to be independent of the fluid grid.

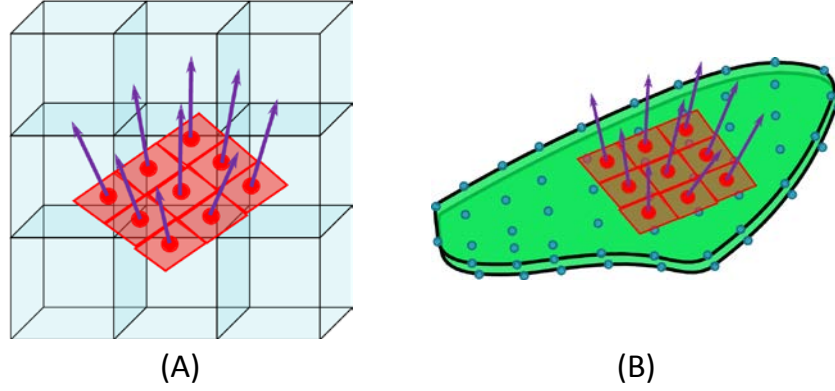


Figure 20: A representative region of fluid particles in the fluid domain, and these same particles in the structural domain. (a) The fluid domain particles are used to represent the kinematics of the body's surface. (b) Likewise, the particles are interpreted by the body as patches of constant applied traction.

A designer of the body would need only to be concerned with sufficient spatial resolution for the body's deformation. This is in contrast to previous immersed boundary implementations. In the work of Vanella, (2010), a rigid wing with the planform of a *Musca domesica* was defined using 381,662 triangles. If each triangle was mapped to the face of a tetrahedron finite element, the number of DOF for a relatively simple body would be staggering. The method implemented here using particles avoids this complication by grouping particles through surface elements. Now a subset of the particles is indexed to a surface element, and this mapping is structured to allow for memory efficiency and calculation speed (Fitzgerald, 2013).

The mapping of each particle to an individual patch of surface on the body is shown in Figure 21. Here $\hat{\mathbf{n}}$ is the outward facing unit vector at center of the patch, and $\{\hat{\mathbf{t}}_1, \hat{\mathbf{t}}_2\}$ is a pair of vectors tangent to the surface. The surface normal is computed by the cross-product of two independent vectors on the surface of the body. To ensure that this calculation results in outward facing normals, a check is performed during mesh pre-processing. The distributed force \mathbf{f}_f is defined in the global frame. The area of each surface patch is A_p . The calculations to determine the kinematics of the deformed surface are performed at the center point of the patch. Since the spacing of particles is the same as the fluid grid, then it is assumed that \mathbf{f}_f is constant on each patch.

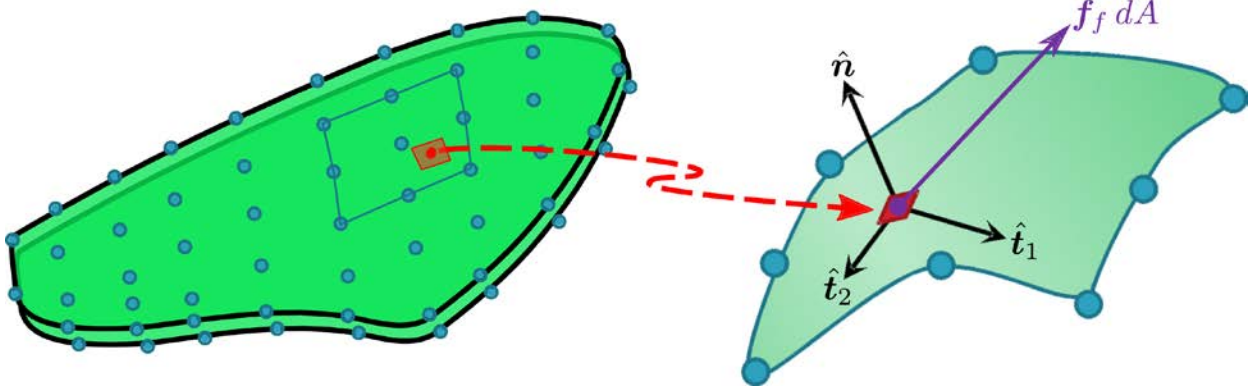


Figure 21: Discrete surface element of the body. The triad $\{\hat{\mathbf{n}}, \hat{\mathbf{t}}_1, \hat{\mathbf{t}}_2\}$ is a local set of unit vectors on the patch p , with differential area dA and surface traction \mathbf{f}_f .

The local ordering of the patches on each element is constructed by using Figure 22. First the length of the deformed element is calculated, and compared with the local fluid grid to determine the spacing of particles on the surface element. There are n_ξ and n_η particles in the ξ -direction and η -direction, respectively. Each particle is assigned a local index p , and this integer is used to uniquely place the patch in the 2D grid (k, j) where $k \in [1, n_\xi] \subset \mathbb{N}$ and $j \in [1, n_\eta] \subset \mathbb{N}$. From there, a unique mapping is defined to identify the index p with all the information needed to consistently integrate the constant surface traction over the patch and project the forces to the element's degrees of freedom. Also this mapping provides all the necessary information to reconstruct the position, velocity, acceleration, deformed area, and outward unit-normal used to impose the no-slip boundary condition on the fluid grid.

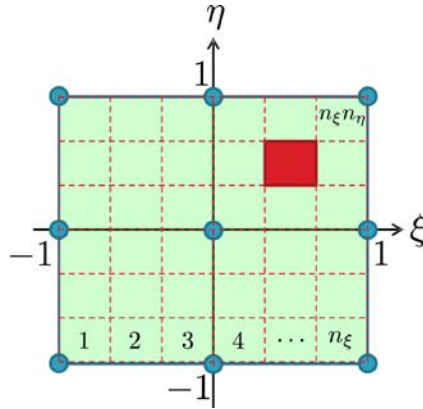


Figure 22: Natural domain of the surface element, showing a single particle patch.

4.4.3 The Generalized- α method

The use of highly resolved finite elements results in both large storage requirements and also in severe time step requirements for explicit integrators. Most finite element integrators use a variant of the seminal Newmark- β method (Newmark, 1959). The Generalized- α method (G- α) is a popular method in the dynamics of linear problems dating back to Chung and Hulbert (1993). It represents a unification of the methods of Hilber *et al.* (1977) and Wood *et al.* (1980), with improved characteristics. The G- α is second order in time, implicit, unconditionally stable for linear problems, and has user selectable dissipation of high frequencies ρ_∞ . It was shown to be suitable for use for nonlinear problems in structural mechanics by Kuhl and co-workers (Kuhl and Crisfield, 1999; Kuhl and Ramm, 1996). A major consequences of using G- α on nonlinear structures is the loss of unconditional stability. A detailed analysis of the properties of the method for simple nonlinear systems can be found in the studies of Baldo *et al.* (2006; Bonelli *et al.* (002), and Erlicher *et al.* (2002).

The method requires only slight modifications to handle essential boundary conditions that are time dependent. The forcing term is modified per \mathbf{h} in (4.10), and it is interpolated with the other external loads and not with the acceleration terms. The implemented G- α in an implicit that is consistently linearized to perform a full Newton-Raphson continuation of the equilibrium of the dynamic equations of motions. The convergence criterion for the Newton-Raphson scheme was chosen to be based on the change to the velocities of the degrees of freedom. This can be stated as

$$\text{error} = \frac{\gamma}{u_{\text{ref}} \beta \Delta t} |\Delta \mathbf{q}|_\infty. \quad (4.11)$$

where γ and β are constants determined by the choice of ρ_∞ . The G- α method is easily adapted for use in the *Structure predictor* and *Structure corrector* roles of Figure 19 with some careful tweaking. There are three main points where discretion is required to use the method efficiently and robustly:

1. The choice of spectral radius ρ_∞ .
2. The choice of the tolerance ε in the Newton-Raphson iterations, and how it should be different between a predictor step and a corrector step in the FSI scheme.
3. The choice of FSI convergence criterion.

The choice of the spectral radius is a body specific problem. Since the radius is relative to the time step a choice of a smaller time step, say for the CFL condition of the fluid, would result in more temporal resolution in the structure. Therefore knowing estimates of the time step that complies with the CFL, and knowing how many modes of the body are likely to be of interest

provides an estimate for the value of ρ_∞ . The bodies considered here, such as flapping wings or moving plates, are mostly undergoing bending deformation similar to their first mode shape. The CFL condition at low Reynolds numbers has a much smaller Δt requirement over the coarse FEM body. Since little excitation of the higher modes are seen, a relatively small value of ρ_∞ is suitable for most of these types of problems.

Changing the value of ε between a prediction step and a correction step was found to be very beneficial to the FSI convergence rate. In the first method explored here, the predictor and corrector are set to only take a single Newton-Raphson step that resulted in FSI substeps in the 40-60 range. A critical review of how the Newton-Raphson iterations take the body from time n to $n+1$ provides the basis for improving on that scheme. For bending problems, the first step of a Newton-Raphson method moves the body in the direction of bending; this makes sense since that is the direction with the lowest stiffness. The subsequent Newton-Raphson shifts the body axially. That first step commonly overestimates the displacement, and the subsequent iterations could be seen as pulling the body back to equilibrium. When the single Newton-Raphson step was used, the convergence rate was impractical since the fluid was reacting to a body that was not close to equilibrium. Using these observations, the Newton-Raphson exit criterion ε can be intelligently changed.

- **Predictor:** Set the value of ε to 1×10^{-9} . This makes the predicted deformation field of the body relatively close to the previous deformation.
- **Corrector:** Set the value of ε to 1×10^{-3} . This allows the Newton-Raphson several substeps before returning to the fluid for an updated set of loads. The overprediction of a single Newton-Raphson step is avoided, and the fluid loads are very current. The structural solver does not waste time being very exact since the fluid loads will change.

The FSI convergence criterion must be set such that the change of the states during a *correction* is less than the tolerance ε_{FSI} ; that is, $\text{error}_{\text{FSI}} \leq \varepsilon_{\text{FSI}}$ where the error is defined as

$$\text{error}_{\text{FSI}} = \left| {}^{(0)}\dot{\mathbf{q}}^{(n+1)} - \dot{\mathbf{q}}^{(n+1)} \right|_{\infty} \quad (4.12)$$

In light of how ε for the corrector is chosen, the condition on FSI must be more strict, $\varepsilon_{\text{FSI}} < \varepsilon$. Therefore, a value of $\varepsilon_{\text{FSI}} = 1 \times 10^{-8}$ is chosen as the default. Also this scheme implies that at least one correction step will always occur which ensures the strong coupling of the equations. During test simulations with the values of ε as stated above, the number of FSI substeps dropped from 40-60 down to 5-8 for the same problem setup. This represents an incredible speed up and opens the possibility of using the method in production simulations.

5 Moving plate example

In order to test the FSI code, a simple and relatively small sized problem was required. Recently, Cleaver *et al.* (2013a, 2013b) performed experiments on compliant plates in a water tunnel. Their force measurements could provide FSI numerical studies with a simple validation case. The problem setup here has been simplified to make the domain manageable for a small number of nodes on the HPC. Here, only 64-128 processors are used with wall times between 12 to 18 hours.

5.1 Formulation

A moving plate of length L , width $0.3L$, and thickness $0.05L$ is centered in a $3L \times 3L \times 3L$ quiescent fluid domain. The plate is rotated 15 degrees along its long axis. The density of the body is varied between $\rho / \rho_{\text{fluid}} \in \{1, 2, 10\}$. The displacements of one of the short edges is restrained by the prescribed kinematics

$$\begin{aligned} x_1(t) &= 0 \\ x_2(t) &= 0 \\ x_3(t) &= (1 - e^{-t/\tau}) A_3 \sin(\omega_f t) \end{aligned} \tag{5.1}$$

where the time constant $\tau = 0.05$ is chosen as a small number to remove an impulsive start but not affect the kinematics for long. The Poisson's ratio was chosen to be 0.3 and Young's modulus was chosen such that the first natural frequency of the body was $\omega_f / \omega_1 = 1/3$. The maximum prescribed velocity is chosen as the reference speed

$$u_{\text{ref}} = \max |\dot{x}_3(t)| = A_3 \omega_f \tag{5.2}$$

The amplitude of oscillation is set to $A_3 = 0.15L$, while the Reynolds number is constructed as

$$\text{Re} = \frac{\rho_{\text{fluid}} L u_{\text{ref}}}{\nu}. \tag{5.3}$$

These parameters are not the same as those used by Cleaver *et al.* (2013a, 2013b), the Reynolds number has been lowered from 10,000, there is no free-stream velocity, and the domain is smaller. The setup tested here is merely a first step and the use of future resources would allow for larger problems that exactly replicates the published work.

5.2 Results

The solution is computed for several periods $T_f = 2\pi / \omega_f$ of forcing. In Figure 23, the surface tractions on a body are shown. From these plots it is clearly evident that even for $Re = 200$, the viscous stresses are mostly quite low, except at the edges of the body. The pressure is acting as one would expect with a large high pressure opposing the motion of the plate.

Computations of the center of mass show how the effect of mass density changes the FSI across different configurations. In Figure 24, the center of mass is shown for densities $\rho / \rho_{\text{fluid}} \in \{10, 2, 1\}$ at $Re = 200$ as well as a dry body. The displacements in x_1 and x_2 appear to change drastically as the density ratio is lowered, and the FSI forces of the fluid begin to dominate the body. This is especially visible in the x_2 direction where the displacements are nearly 10 times those of the dry (non-FSI) case. The fluid also appears to be damping out the higher frequencies of the response. This is seen in the x_3 direction, where only the dry body appears to have multiple frequencies in the response.

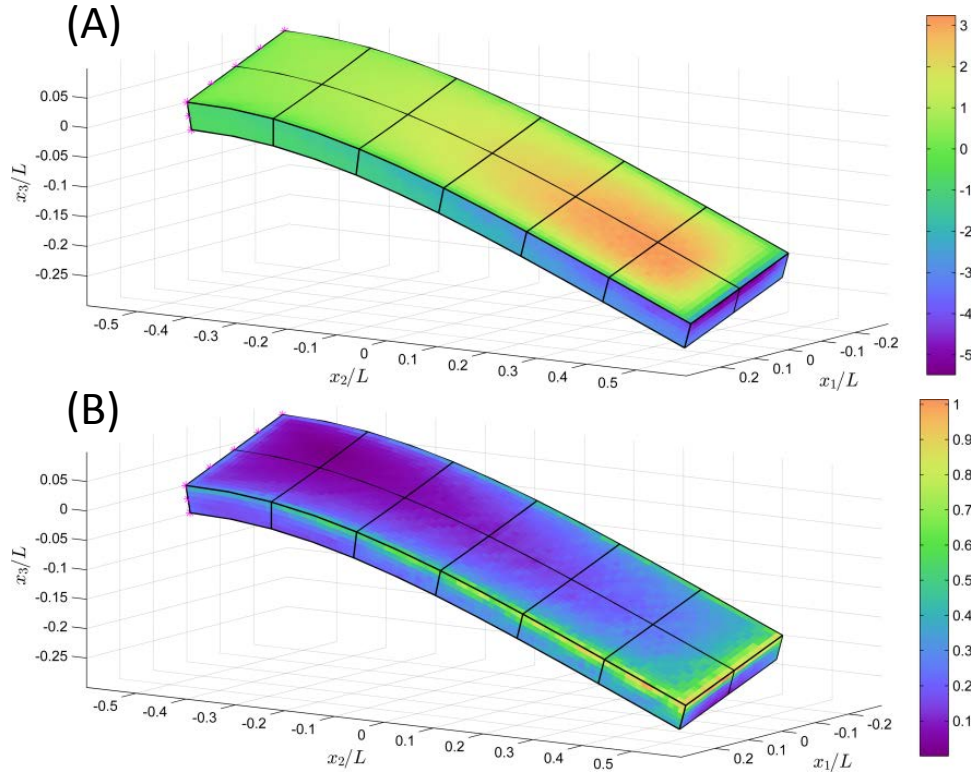


Figure 23: Example of the surface stresses acting on the body. These are the instantaneous values at $t / T_f = 2.05$, for $Re = 200$, $\rho / \rho_{\text{fluid}} = 1$. (A) Pressure on the body, with colors corresponding to $C_p / 2$. (B) Magnitude of the viscous stress, with colors corresponding to $C_\mu / 2$.

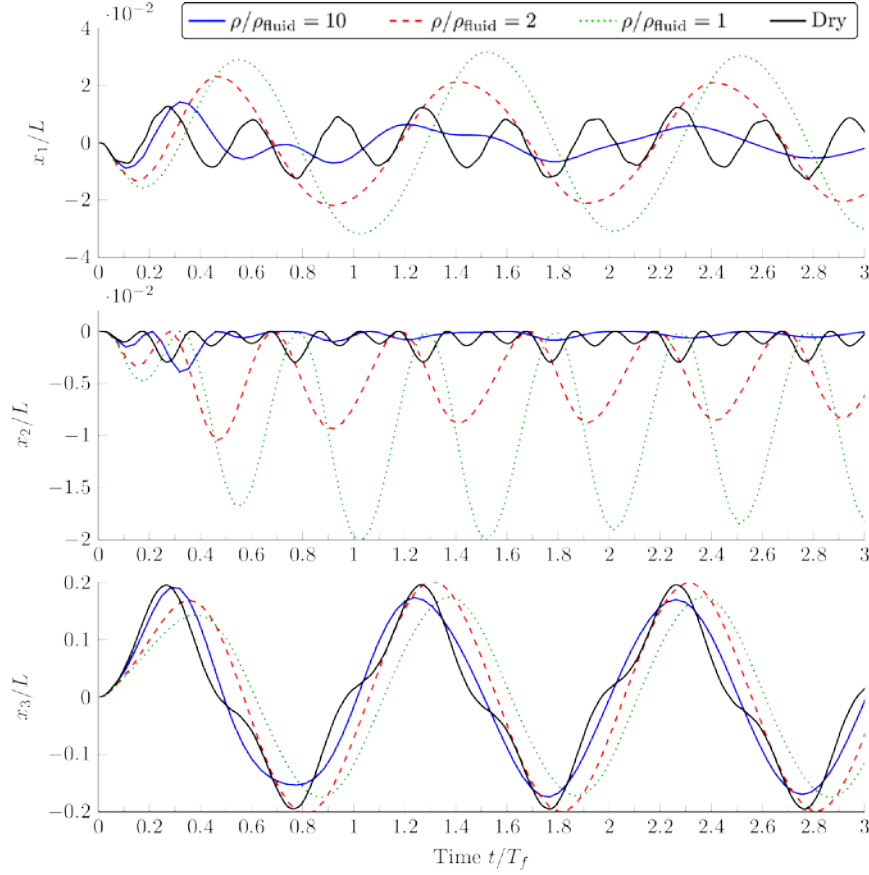


Figure 24: Position of the center of mass in the deformable plate for $Re = 200$.

Integrating the surface stresses across the body provides a way to compare the fluid contributions across the density range. The total force due to viscous stresses is quite small for all time in Figure 25. This correlates well to the instantaneous field shown in Figure 23B where the peaks may have been large, but they were highly localized. The pressure forces are dominating in all three directions by an order of magnitude.

The visualization of the flow fields of Figure 26 were constructed by using TecPlot. At several instances of time, a number of isocontours of the Q-criterion (Hunt *et al.*, 1988) are plotted along with a x_2 - x_3 slice of the x_3 velocity field. Depicted in the left column are results for $Re = 200$, and in the right column are $Re = 1000$ at nearly the same instances of time. The density ratio of the body is $\rho/\rho_{\text{fluid}} = 1$, which as demonstrated in the previous figures results in the largest deformation and highest loads. The Q-isosurfaces are not symmetric about the x_2 - x_3 plane since the body is rotated along the x_2 -axis. Comparing side-by-side frames shows that the flow structures appear smaller and remain longer as the Reynolds number is increased. At $t/T_f = 1.61$ for $Re = 1000$ the Q-isosurface appears to be rolling up on itself in a hairpin-like

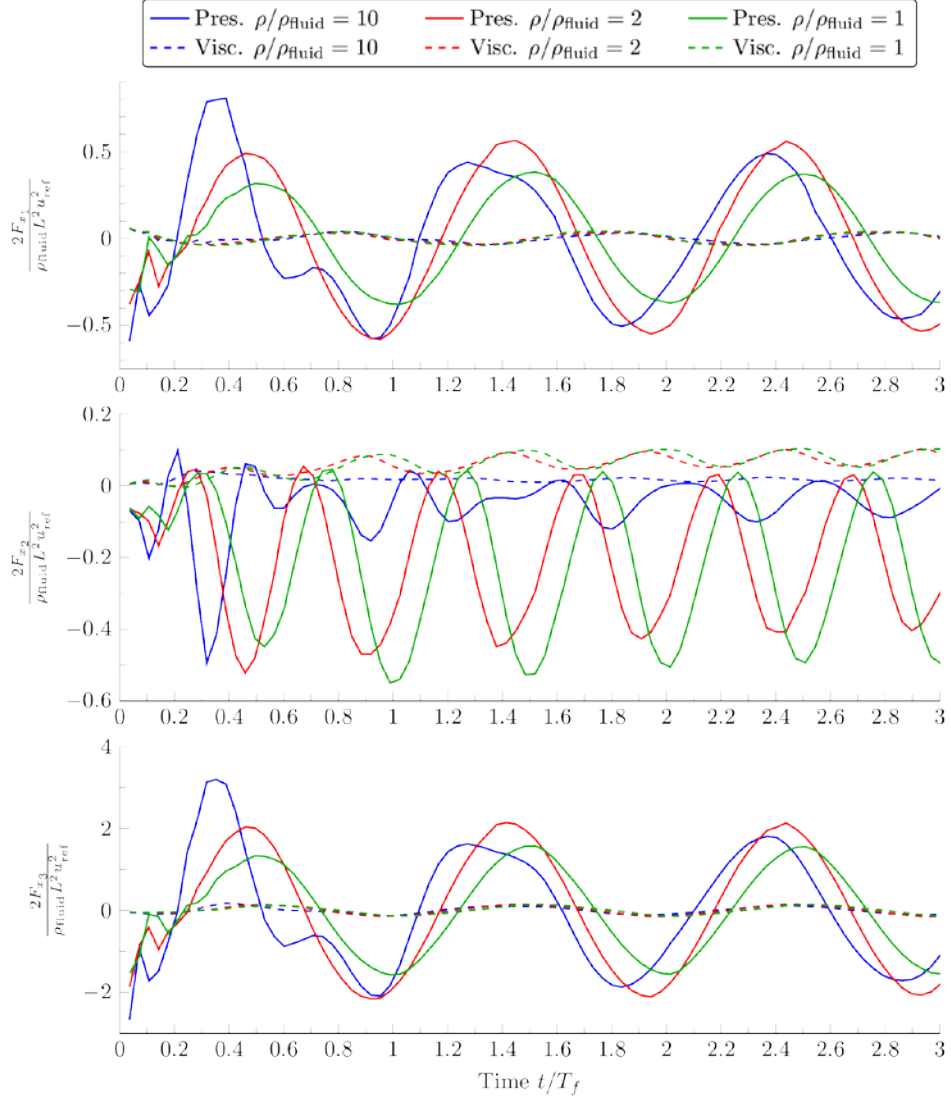


Figure 25: Fluid forces computed at the centroid of the deformable plate for $Re = 200$.

manner (Bernard, 2011). Overall, the results from these tests appear promising. The FSI algorithm works efficiently enough to make serious problems practical for calculations. This is assuming that the necessary HPC power is available.

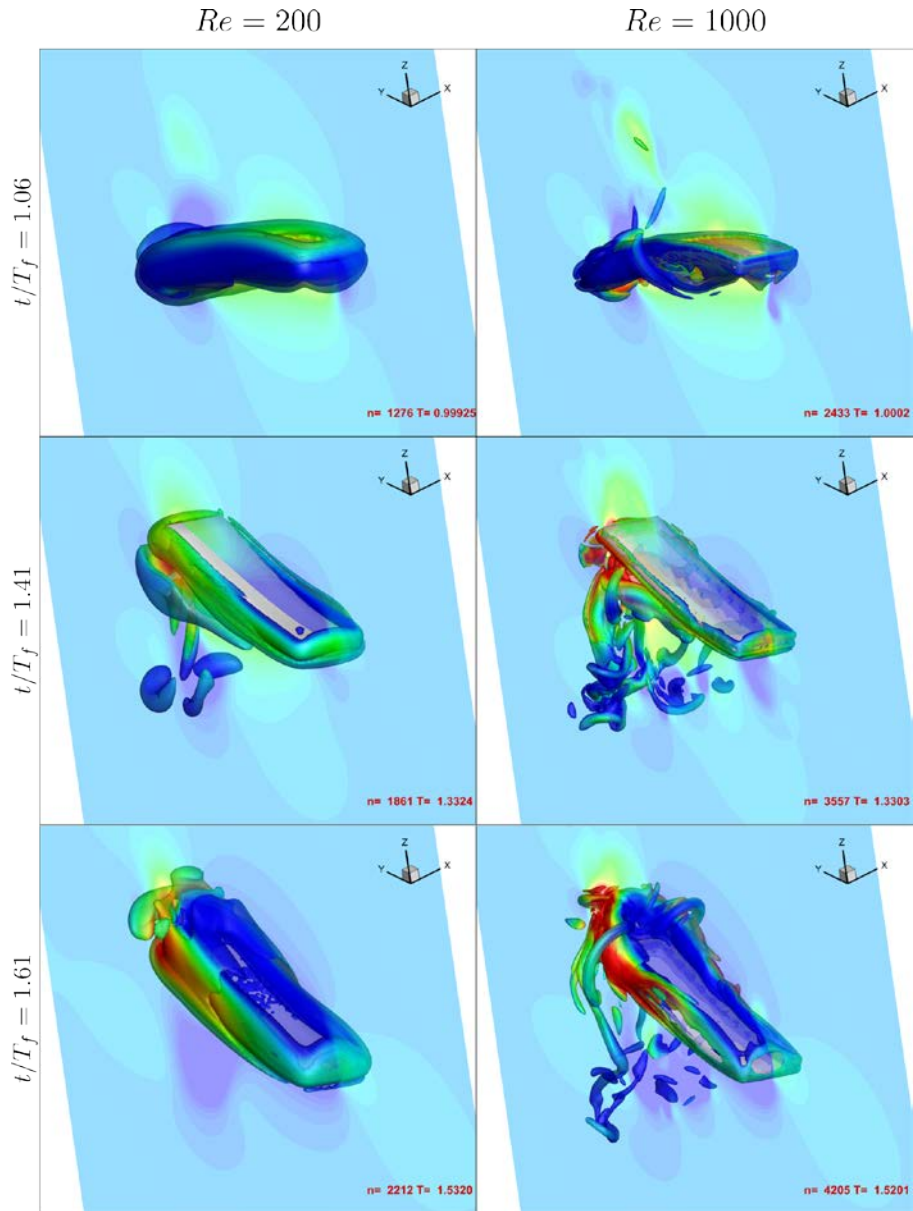


Figure 26: Demonstration of FSI for a flexible plate with $\rho / \rho_{\text{fluid}} = 1$, and $\omega_f / \omega_1 = 1/3$. The time has been nondimensionalized with T_f . Shown are isosurfaces of the Q-criterion and a slice of the z velocity in the $y-z$ plane.

6 Concluding Remarks

6.1 Future work

The next steps are to validate the implemented FSI code by using the experiments of Cleaver *et al.* (2013a, b) and use the code to simulate flexible wings. The first insect inspired geometry to be modeled is the forewing of a *Manduca sexta*. In Figure 27, the researchers show the first draft of a 3D FEM mesh of the planform. This shape was extracted from a figure provided in the work of O'Hara and Palazotto (2012). Another useful reference for wing planforms is the work of Comstock (1918), which contains many illustrations.

The driving kinematics can be based on the functions discussed by Berman and Wang (2007). Their angular description of flapping motion is applicable to a broad range of flapping styles. The hawkmoth parameters of Berman and Wang (2007) suggest an almost constant angle of attack for the majority of the hover stroke with relatively fast reversals at the ends of the stroke. This kinematics has been implemented in the FLASH code and illustrated in Figure 28 by using the parameters provided by Berman and Wang (2007) for the hawkmoth.

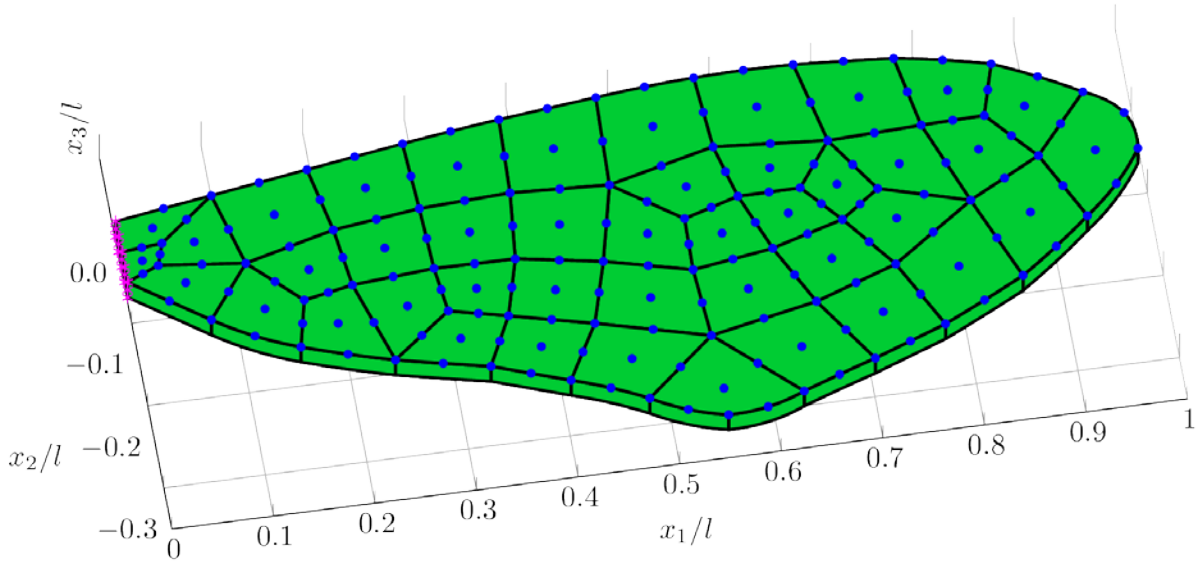


Figure 27: Mesh of a *Manduca sexta* inspired wing. The planform is based on the results of O'Hara and Palazotto (2012). The restrained nodes are at the root in magenta. The free nodes are shown in blue (only the top surface is shown for clarity).

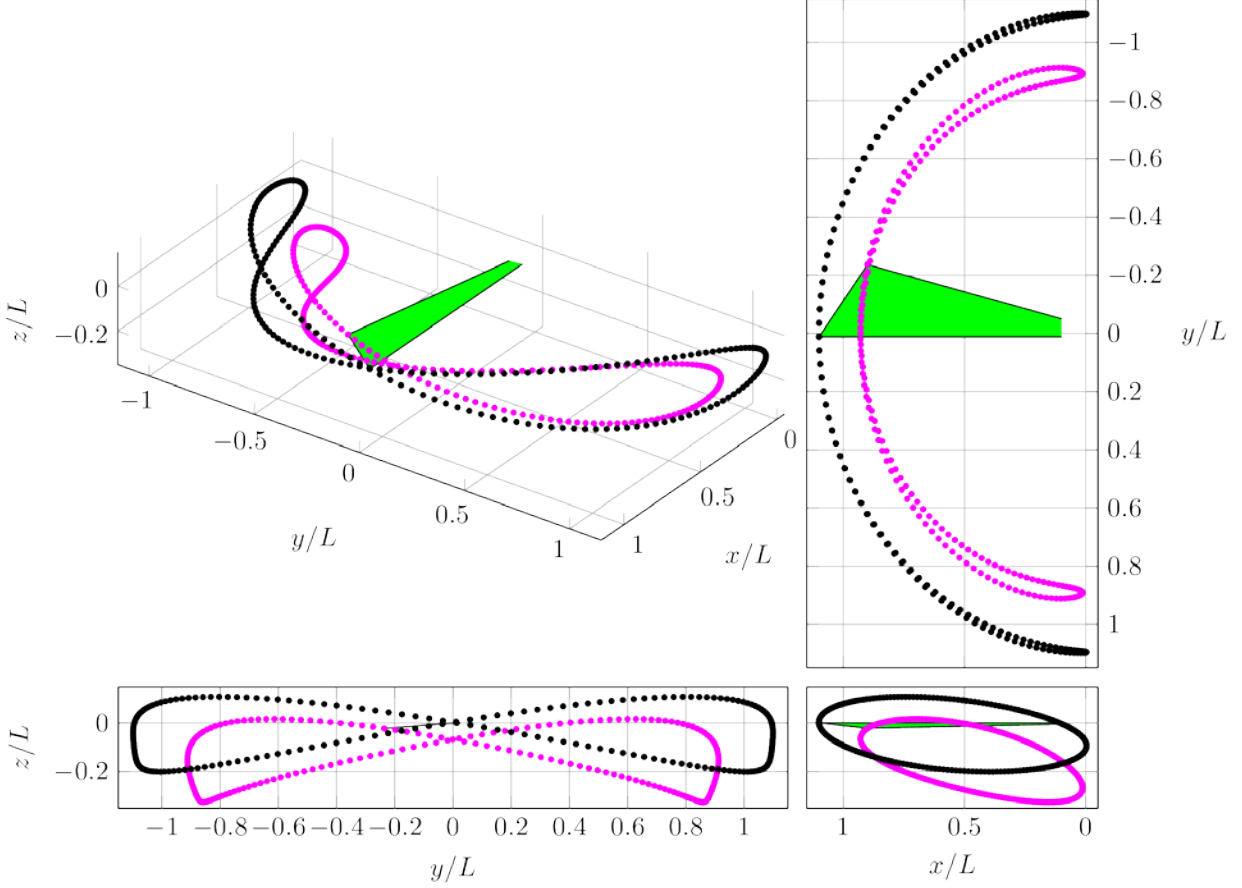


Figure 28: Demonstration of the implemented kinematics employing the hawkmoth parameters from Berman and Wang (2007).

Preliminary dry tests with $\omega_f / \omega_n = 1/3$ for a homogeneous body indicate that the body is too soft. A realistic correction is stiffening of the root and leading edge of the wing. This follows from the spirit of the parameter distribution proposed by Combes and Daniel (2003a) as well as the mode shapes found in §4.2.

The Reynolds number of a *Manduca sexta* based on the span length and peak tip speed would be in the range of $25 \times 10^3 - 29 \times 10^3$. This increase in Reynolds number drastically changes the computing requirements for a practical simulation. If uniform grids are used for example, assuming that the cell size would need to be approximately $\Delta x = 0.002L$, then a *small* domain of $4L \times 4L \times 4L$ would have roughly 2048^3 points. If the FLASH block size is 32^3 , this results in 64^3 blocks to distribute on a HPC. For this sized blocks, it was found that placing more than 30 blocks per processor results in poor scaling. Therefore, 216,224 blocks at 30 blocks per processor results in 8,739 processors. That many processors represent a major use of resources,

and this need is beyond the clusters currently available at the University of Maryland. The use of AMR and lower Reynolds number cases will need to be considered as the next practical steps.

6.2 Outcomes

- **Wing flexibility**: The models that capture the physics of flapping flight in 2D were developed and analyzed. It was shown that under assumptions moderate flexibility is beneficial.
- **Model fidelity**: A comparison study between DNS and UVLM in 2D demonstrated the range of usefulness of the computationally inexpensive UVLM. This comparative study indicates that the UVLM is well suited to determine *averaged* quantities, such as those that would be used in an objective function for optimization of design variables. Subsequent investigations around the design point using the DNS would still be required to ensure the desired results.
- **Insect wing experiments**: A novel experiment to measure the vibration characteristics of a living hawkmoth was conducted. These findings correlate well to the work of Sims (2010) and provide information to support the 1/3 harmonic forcing found in nature.
- **High fidelity computation**: Since the physics of flapping flight in 3D is less well-known, the uses of low-fidelity models are not yet reliable. This led the researchers to build a high-performance FSI code built into the FLASH framework.
- **Partitioned FSI algorithm**: A novel partitioned FSI algorithm using the Generalized- α method is described. This method is suitable for large scale systems, with bodies of tens of thousands of degrees of freedom. Special attention is given to the time step requirements, and how this method decouples the fluid grid generation from the body mesh generation. A consistent method to project the boundary conditions between the body and the fluid is constructed using the Lagrangian markers in the PARTICLES unit of FLASH.
- **Three-dimensional studies with a flexible body**: The highly flexible 3D FSI code has been demonstrated as operational, and algorithmically tuned. The numerical demonstrations of the above methods show the effectiveness of the algorithms and implementations. A fully flexible plate is excited in a flow over a range of densities and Reynolds numbers. It was found that the methods worked well, even for equal densities between the fluid and the solid. Large deformations were handled without issue by only 12 elements, and the FSI substeps were kept low (between 5 to 8).

7 References

- ASC Flash Center, 2012. FLASH User's Guide. University of Chicago.
- Baldo, G., Bonelli, A., Bursi, O., and Erlicher, S., 2006. The accuracy of the generalized- α method in the time integration of non-linear single- and two-DOF forced systems. *Comput. Mech.* 38, 15–31. doi:10.1007/s00466-005-0718-x.
- Belytschko, T., Liu, W. K., and Moran, B., 2000. *Nonlinear finite elements for continua and structures*. Wiley.
- Berman, G. J. and Wang, Z.J., 2007. Energy-minimizing kinematics in hovering insect flight. *J. Fluid Mech.* 582, 153–168. doi:10.1017/S0022112007006209.
- Bernard, P.S., 2011. The hairpin vortex illusion. *J. Phys. Conf. Ser.* 318, 062004. doi:10.1088/1742-6596/318/6/062004.
- Bonelli, A., Bursi, O.S., Erlicher, S., and Vulcan, L., 2002. Analyses of the generalized- α method for linear and non-linear forced excited systems, in: *Structural Dynamics-EURODYN 2002*. Munich, Germany, pp. 1523–1528.
- Chung, J. and Hulbert, G.M., 1993. A Time Integration Algorithm for Structural Dynamics With Improved Numerical Dissipation: The Generalized- α Method. *J. Appl. Mech.* 60, 371–375. doi:10.1115/1.2900803.
- Cleaver, D., Calderon, D. E., Wang, Z. J., and Gursul, I., 2013a. Low Aspect Ratio Oscillating Flexible Wings at Low Reynolds Numbers, in: *43rd Fluid Dynamics Conference*. AIAA, San Diego, CA. doi:10.2514/6.2013-3178.
- Cleaver, D., Wang, Z. J., and Gursul, I., 2013b. Oscillating Flexible Wings at Low Reynolds Numbers, in: *51st AIAA Aerospace Sciences Meeting Including the New Horizons Forum and Aerospace Exposition*. AIAA, Grapevine (Dallas/Ft. Worth Region), Texas. doi:10.2514/6.2013-674.
- Combes, S. A. and Daniel, T. L., 2003a. Flexural stiffness in insect wings II. Spatial distribution and dynamic wing bending. *J. Exp. Biol.* 206, 2979–2987. doi:10.1242/jeb.00524.
- Combes, S. A. and Daniel, T. L., 2003b. Into thin air: contributions of aerodynamic and inertial-elastic forces to wing bending in the hawkmoth *Manduca sexta*. *J. Exp. Biol.* 206, 2999–3006. doi:10.1242/jeb.00502.
- Combes, S. A. and Daniel, T. L., 2003c. Flexural stiffness in insect wings I. Scaling and the influence of wing venation. *J. Exp. Biol.* 206, 2979–2987. doi:10.1242/jeb.00523.
- Comstock, J. H., 1918. *The wings of insects*. Comstock Publishing Company, Ithaca, New York.
- Daley, C., Vanella, M., Dubey, A., Weide, K., and Balaras, E., 2012. Optimization of multigrid based elliptic solver for large scale simulations in the FLASH code. *Concurr. Comput. Pract. Exp.* 24, 2346–2361. doi:10.1002/cpe.2821.

- Erlicher, S., Bonaventura, L., and Bursi, O. S., 2002. The analysis of the Generalized- α method for non-linear dynamic problems. *Comput. Mech.* 28, 83–104. doi:10.1007/s00466-001-0273-z.
- Fitzgerald, T., 2013. Nonlinear fluid-structure interactions in flapping wing systems, PhD Dissertation, University of Maryland, College Park, MD.
- Fitzgerald, T., Valdez, M., Vanella, M., Balaras, E., and Balachandran, B., 2011. Flexible Flapping Systems: Computational Investigations into Fluid-Structure Interactions. *Aeronaut. J.* 115.
- Geuzaine, C. and Remacle, J.-F., 2009. Gmsh: A 3-D finite element mesh generator with built-in pre- and post-processing facilities. *Int. J. Numer. Methods Eng.* 79, 1309–1331. doi:10.1002/nme.2579.
- Herbert, R.C., 2001. Modelling insect wings using the finite element method. University of Exeter.
- Hilber, H.M., Hughes, T. J. R., and Taylor, R. L., 1977. Improved numerical dissipation for time integration algorithms in structural dynamics. *Earthq. Eng. Struct. Dyn.* 5, 283–292. doi:10.1002/eqe.4290050306.
- Holmes, P., Lumley, J. L., and Berkooz, G., 1996. Turbulence, Coherent Structures, Dynamical Systems and Symmetry. Cambridge University Press.
- Hughes, T.J.R., 2000. The Finite Element Method: Linear static and dynamic finite element analysis. Dover.
- Hunt, J.C.R., Wray, A.A., and Moin, P., 1988. Eddies, streams, and convergence zones in turbulent flows, in: The Proceedings of the 1988 Summer Program. Center for Turbulence Research, Stanford University, pp. 193–208.
- Kang, C.-K., Aono, H., Cesnik, C. E. S., and Shyy, W., 2011. Effects of flexibility on the aerodynamic performance of flapping wings. *J. Fluid Mech.* 689, 32–74. doi:10.1017/jfm.2011.428.
- Kim, J. and Moin, P., 1985. Application of a fractional-step method to incompressible Navier-Stokes equations. *J. Comput. Phys.* 59, 308–323. doi:10.1016/0021-9991(85)90148-2.
- Kuhl, D. and Crisfield, M.A., 1999. Energy-conserving and decaying Algorithms in non-linear structural dynamics. *Int. J. Numer. Methods Eng.* 45, 569–599. doi:10.1002/(SICI)1097-0207(19990620)45:5<569::AID-NME595>3.0.CO;2-A.
- Kuhl, D. and Ramm, E., 1996. Constraint energy momentum algorithm and its application to non-linear dynamics of shells. *Comput. Methods Appl. Mech. Eng.* 136, 293–315. doi:10.1016/0045-7825(95)00963-9.
- MacNeice, P., Olson, K.M., Mobarry, C., de Fainchtein, R., and Packer, C., 2000. PARAMESH: A parallel adaptive mesh refinement community toolkit. *Comput. Phys. Commun.* 126, 330–354. doi:10.1016/S0010-4655(99)00501-9.

- Newmark, N. M., 1959. A method of computation for structural dynamics. *J. Eng. Mech. Div. ASCE* 85, 67–94.
- O'Donnell, B. J. and Helenbrook, B. T., 2007. Proper orthogonal decomposition and incompressible flow: An application to particle modeling. *Comput. Fluids* 36, 1174–1186. doi:10.1016/j.compfluid.2006.12.004.
- O'Hara, R. P. and Palazotto, A. N., 2012. The morphological characterization of the forewing of the *Manduca sexta* species for the application of biomimetic flapping wing micro air vehicles. *Bioinspir. Biomim.* 7, 046011. doi:10.1088/1748-3182/7/4/046011.
- Pai, P. F., Chernova, D. K., and Palazotto, A.N., 2009. Nonlinear Modeling and Vibration Characterization of MAV Flapping Wings, in: 50th AIAA/ASME/ASCE/AHS/ASC Structures, Structural Dynamics, and Materials Conference. Palm Springs, California. doi:10.2514/6.2009-2415.
- Preidikman, S., 1998. Numerical simulations of interactions among aerodynamics, structural dynamics, and control systems. PhD Dissertation, Virginia Polytechnic Institute and State University, Blacksburg, VA.
- Sims, T.W., 2010. A structural dynamic analysis of a *Manduca Sexta* forewing, MS Thesis, Air Force Institute of Technology, Wright-Patterson AFB, OH.
- Sirovich, L., 1987. Turbulence and the dynamics of coherent structures. Part I: Coherent Structures. *Q. Appl. Math.* 45, 561–571.
- Valdez, M., 2008. Unsteady Vortex Lattice Method Code, University of Maryland, College Park, MD.
- Valdez, M., Preidikman, S., and Massa, J. C., 2006. Aerodinámica De Flujos Bidimensionales E. Inestacionarias Dominados Por Vorticidad. *Mecánica Comput.* 25, 2333–2357.
- Vanella, M., 2010. A fluid structure interaction strategy with application to low Reynolds number flapping flight. PhD Dissertation, University of Maryland, College Park, MD.
- Vanella, M., Fitzgerald, T., Preidikman, S., Balaras, E., and Balachandran, B., 2009. Influence of flexibility on the aerodynamic performance of a hovering wing. *J. Exp. Biol.* 212, 95–105. doi:10.1242/jeb.016428.
- Wang, Z. J., Birch, J. M., and Dickinson, M.H., 2004. Unsteady forces and flows in low Reynolds number hovering flight: two-dimensional computations vs robotic wing experiments. *J. Exp. Biol.* 207, 449–460. doi:10.1242/jeb.00739.
- Weis-Fogh, T., 1973. Quick Estimates of Flight Fitness in Hovering Animals, Including Novel Mechanics for Lift Production. *J. Exp. Biol.* 59, 169–230.
- Wood, W. L., Bossak, M., and Zienkiewicz, O.C., 1980. An alpha modification of Newmark's method. *Int. J. Numer. Methods Eng.* 15, 1562–1566. doi:10.1002/nme.1620151011.
- Wootton, R. J., 1992. Functional Morphology of Insect Wings. *Annu. Rev. Entomol.* 37, 113–140. doi:10.1146/annurev.en.37.010192.000553

Yang, J., Preidikman, S., and Balaras, E., 2008. A strongly coupled, embedded-boundary method for fluid-structure interactions of elastically mounted rigid bodies. *J. Fluids Struct.* 24, 167–182. doi:10.1016/j.jfluidstructs.2007.08.002.

Zhao, L., Huang, Q., Deng, X., and Sane, S. P., 2010. Aerodynamic effects of flexibility in flapping wings. *J. R. Soc. Interface* 7, 485–497. doi:10.1098/rsif.2009.0200.